JGR Atmospheres

RESEARCH ARTICLE
10.1029/2023JD039794

Key Points:

- The annual isotopic composition of precipitation on Réunion Island is controlled by the number of cyclones per year
- Both precipitation and water vapor are systematically more depleted during cyclonic periods
- More large-scale precipitation and rain–vapor interactions are responsible for the stronger isotopic depletion during tropical cyclones (TCs)

Supporting Information:

Supporting Information may be found in the online version of this article.

Correspondence to:

F. Vimeux,
Francoise.Vimeux@lsce.ipsl.fr

Citation:

Vimeux, F., Risi, C., Barthe, C., François, S., Cauquoin, A., Jossoud, O., et al. (2024). Is the isotopic composition of precipitation a robust indicator for reconstructions of past tropical cyclones frequency? A case study on Réunion Island from rain and water vapor isotopic observations. *Journal of Geophysical Research: Atmospheres*, *129*, e2023JD039794. https://doi.org/10.1029/2023JD039794

Received 9 AUG 2023
Accepted 12 JAN 2024

Is the Isotopic Composition of Precipitation a Robust Indicator for Reconstructions of Past Tropical Cyclones Frequency? A Case Study on Réunion Island From Rain and Water Vapor Isotopic Observations

Françoise Vimeux[1,2], Camille Risi[3], Christelle Barthe[4], Sören François[2], Alexandre Cauquoin[5], Olivier Jossoud[2], Jean-Marc Metzger[6], Olivier Cattani[2], Bénédicte Minster[2], and Martin Werner[7]

[1]HydroSciences Montpellier (HSM), UMR 5151 (Université Montpellier, CNRS, IMT, IRD), Montpellier, France, [2]Institut Pierre Simon Laplace (IPSL), Laboratoire des Sciences du Climat et de l'Environnement (LSCE), UMR 8212 (CEA, CNRS, UVSQ), Gif-sur-Yvette, France, [3]Institut Pierre Simon Laplace (IPSL), Laboratoire de Météorologie Dynamique (LMD), UMR 8539 (CNRS, ENS, X, UPMC), Paris, France, [4]Laboratoire d'Aérologie (LAERO), UMR 5560 (CNRS, UT3 Paul Sabatier, IRD), Toulouse, France, [5]Institute of Industrial Science (IIS), The University of Tokyo, Kashiwa, Japan, [6]Observatoire des Sciences de l'Univers de la Réunion, UAR 3365 OSU-R (CNRS, Université de la Réunion), Saint-Denis de La Réunion, France, [7]Alfred Wegener Institute (AWI), Helmholtz Centre for Polar and Marine Research, Bremerhaven, Germany

Abstract Based on a 6-year long record (2014–2020) of the isotopic composition of rain ($\delta^{18}O_p$) at Réunion Island (55°E, 22°S), in the South-West Indian Ocean, this study shows that the annual isotopic composition of precipitation in this region is strongly controlled by the number of cyclones, the number of best-track days, and the proportion of cyclonic rain during the year. Our results support the use of $\delta^{18}O_p$ in annual-resolved tropical climate archives as a reliable proxy of past cyclone frequency. The influence of the proportion of cyclonic rain on the annual isotopic composition arises from the systematically more depleted precipitation and water vapor during cyclonic events than during less organized convective systems. The analysis of the daily to hourly isotopic composition of water vapor ($\delta^{18}O_v$) during low-pressure systems and the reproduction of daily $\delta^{18}O_v$ observations by AGCMs with a global medium to coarse resolution (LMDZ-iso and ECHAM6-wiso) suggest that during cyclonic periods the stronger depletion mainly arises from both enhanced large-scale precipitation and water vapor-rain interactions under humid conditions.

Plain Language Summary Water molecules have different forms: 2 atoms of hydrogen and 1 atom of oxygen 16 (majority form), or 1 atom of hydrogen, 1 atom of deuterium (^2H) and 1 atom of oxygen 16, or 2 atoms of hydrogen and 1 atom of oxygen 18. The relative proportion of these different molecules in precipitation and water vapor is called isotopic composition. We have analyzed the isotopic composition of rain and water vapor at Réunion Island (55°E, 22°S), in the South-West Indian Ocean, for 6 years (2014–2020). We show that the annual isotopic composition of precipitation in this region is a reliable indicator of the number of tropical cyclones (TCs) during the year. This opens the possibility to use annual-resolved tropical climate archives of the isotopic composition of precipitation, like speleothems, to study how cyclone frequency in the Indian Ocean has varied in the past under different mean climates (warmer or colder). This study also seeks to understand why the isotopic composition of precipitation behaves in this way during TCs. We show that this is due to increased precipitation at the regional scale and enhanced exchanges of water molecules between rain and water vapor in the vicinity of TCs.

1. Introduction

Tropical cyclones (TCs) are among the natural hazards responsible for the highest human and economic losses. According to the WMO (World Meteorological Organization), 7 of the 10 costliest natural disasters in the past 50 years are TCs, including three cyclones in 2017: Harvey (which caused nearly $97 billion in damage), Maria (nearly $70 billion) and Irma (nearly $60 billion) (WMO, 2021). These three cyclones alone accounted for 35% of the total economic losses of the top 10 disasters around the world from 1970 to 2019. The cyclone Katrina in 2005 stands out as the costliest disaster with nearly $164 billion in losses. In terms of human losses, the 10 deadliest natural disasters between 1970 and 2019 include 3 TCs: in Bangladesh in 1970 (cyclone Bhola) and in 1991

(cyclone Gorky), resulting in approximately 439,000 deaths, and in Myanmar in 2008 (cyclone Nargis), resulting in more than 138,000 deaths (WMO, 2021).

TCs are projected to become more intense with global warming (Bloemendaal et al., 2022 for the most recent reference and references herein). The average and maximum rain rates associated with TCs are expected to increase in a warming world (IPCC, 2021, Chapter 11.7.1). The median projected increase of TC rain rates at the global scale is about 11% (28%) for a global warming of +1.5°C (+4°C) (Seneviratne et al., 2021, Table 11.2). However, uncertainties remain surrounding the long-term change in TC frequency although most, but not all, high-resolution global simulations project a reduction in the total global number of TCs (Knutson et al., 2020). As a consequence, the last IPCC WG1 report concluded, with a medium confidence level, that the number of TCs is expected to decrease or to remain unchanged (IPCC, 2021).

The issue of how TCs frequency responds to climate change can be addressed with paleo-tempestology. The latter aims to offer reconstructions of past TC activity from archives of the isotopic composition of rain ($\delta^{18}O_p$). Indeed, previous studies have shown that cyclonic rains have a specific isotopic signature. They exhibit a much more depleted isotopic composition than rain produced by monsoon systems for similar precipitation rate (Ansari et al., 2020; Gedzelman et al., 2003; Munksgaard et al., 2015). In this line, some studies have investigated this specific isotopic signature of cyclonic rains in speleothems to propose reconstructions of past cyclone activity (Baldini et al., 2016; Chen et al., 2021; Frappier et al., 2007). However, previous studies dealing with the comparison between cyclonic and non-cyclonic $\delta^{18}O_p$ rely on observations obtained on one site and over one or a few TCs with no inter-annual perspective and with no quantification of how TCs impact annual $\delta^{18}O_p$.

In this paper, we examine the isotopic composition of both precipitation and near-surface water vapor recorded during between 2014 and 2020 on Réunion Island (encompassed between 55.20°E and 55.85°E and 20.85°S and 21.40°S), a French island in the South-West Indian Ocean. The originality of this dataset is to gather a panel of cyclones and thunderstorms with different maturity, intensity, trajectory, lifetime, structure, rainfall amount and position relative to Réunion Island, that were sampled on the same site in the framework of a 6-year long continuous monitoring of the isotopic composition of both water vapor and rain. It is worth noting that the site of Réunion Island has not been investigated in previous isotopic studies dedicated to TCs whereas it is a hot spot for cyclonic activity (Leroux et al., 2018).

We first explore how the presence of cyclonic rains within a year affects the annual and the seasonal isotopic composition of precipitation and how the amount effect, that is, the decrease of $\delta^{18}O_p$ as precipitation rate increases, is affected by the cyclonic nature of the rain. The availability of a 6-year long data set also enables us to discuss whether the inter-annual variability of the isotopic composition of precipitation can be a correct candidate to reconstruct inter-annual variations of the cyclonic season characteristics (number and duration of cyclones, proportion of cyclonic rain).

Then, to go further, based on daily to hourly isotopic observations and on daily outputs from atmospheric general circulation models (AGCMs) equipped with water stable isotopes, we try to understand what could be the large-scale and the mesoscale atmospheric processes responsible for the specific isotopic signature of cyclonic rains.

2. Data and Methods

2.1. Observations at the Maïdo Site

The isotopic composition of near-surface water vapor ($\delta^{18}O_v$ and δD_v in ‰ vs. SMOW) and the water vapor mixing ratio (q_v in ppmv that we translate in g/kg of dry air, see Tremoy et al., 2011) have been measured continuously since 1 November 2014 at the Maïdo atmospheric observatory (21.079°S, 55.383°E, 2160 m a.s.l.; Baray et al., 2013) on Réunion Island (Figure 1). The time period of interest in this paper is from 1 November 2014 to 31 October 2020. The measurements have been done with a Picarro Inc. instrument (L2130-I model) based on wavelength-scanned cavity ring down spectroscopy. The detailed protocol for measurements and the corrections applied on raw data can be found in Guilpart et al. (2017). The short-term precision of the instrument ($\pm 1\sigma$) during a 10-min stable injection of water isotopic standard is better than ±0.02‰ and ±0.09‰ for $\delta^{18}O_v$ and δD_v respectively, leading to a quadratic accuracy better than ±1.8‰ for deuterium excess (d_v) (Dansgaard, 1964). The recorded gaps in the series are due to instrument calibrations and to power cuts.

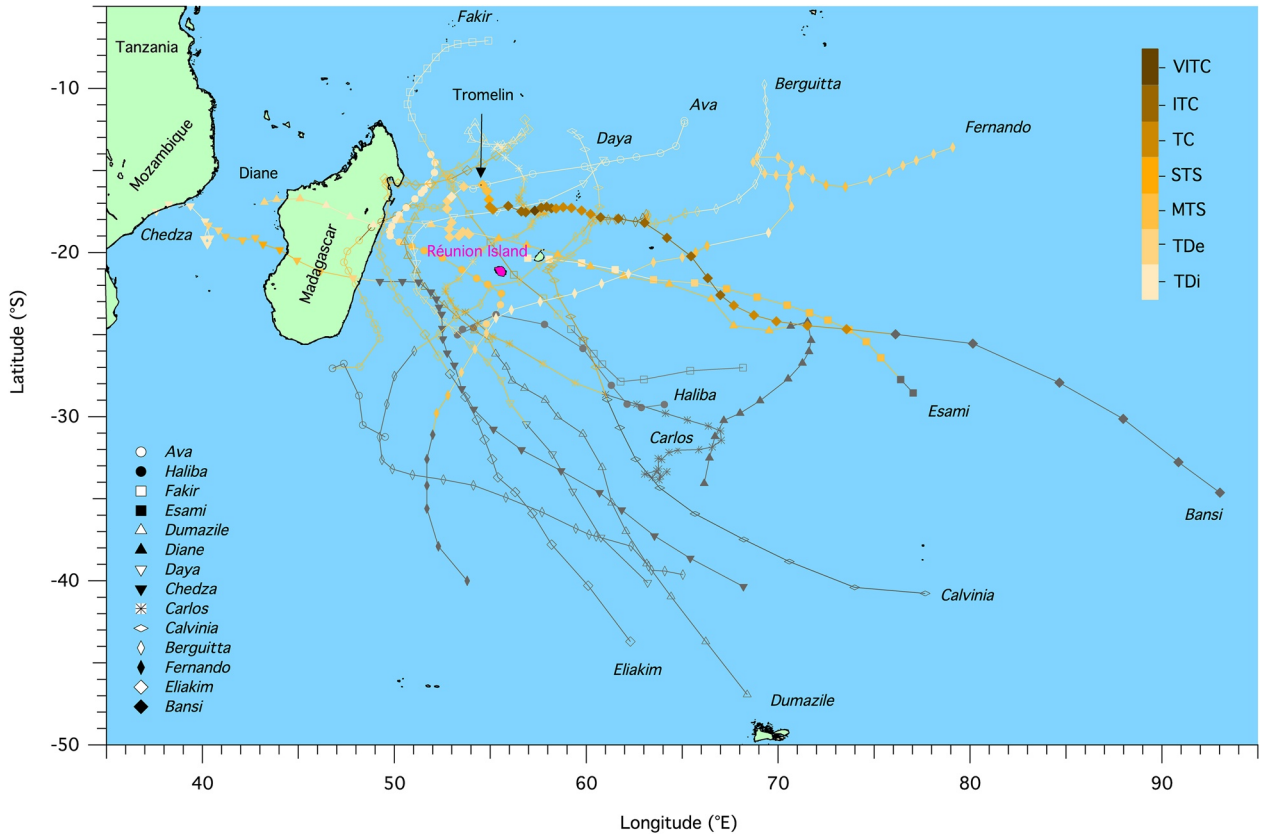

Figure 1. Trajectories over the best-track periods for the 14 systems identified in Table 1. Names of the cyclone are plotted at the start or at the end of trajectories, and symbols are placed along the trajectory at 6-hr intervals. The color scale (7 levels) indicates the RSMC best-track classification as mentioned in Table 1. The final stages for the systems identified in the RSMC best-track classification (post-tropical, extra-tropical, residual, filling up, and dissipating) are shown in gray. The shorelines data was extracted from the GNOME Online Oceanographic Data Server (https://gnome.orr.noaa.gov/goods/tools/GSHHS/coast_subset).

Table 1
RSMC Classification for the Storms and the Cyclonic Systems Based on the Maximum 10-Min Average Surface Wind Speed (V_{max_10min} in Knot, 1 Knot = 1.852 km/hr)

Classification	Acronym	V_{max_10min} (knot)
Tropical disturbance	TDi	$v < 27$
Tropical depression	TDe	$28 < v < 33$
Moderate tropical storm	MTS	$34 < v < 47$
Severe tropical storm	STS	$48 < v < 63$
Tropical cyclone	TC	$64 < v < 89$
Intense tropical cyclone	ITC	$90 < v < 115$
Very intense tropical cyclone	VITC	$v > 115$

Precipitation has been collected at the Maïdo atmospheric observatory on an event-based scheme to analyze its isotopic composition ($\delta^{18}O_p$ and δD_p in ‰ vs. SMOW). We used a SPIEA pluviometer (approved by Météo-France) with a direct measurement of precipitation amount. The rain was collected right after the rain event. Unfortunately, during the most intense phase of cyclonic periods, because of local restrictions on travel, the rain could not be collected on an event-based scheme. For these specific periods, we used a cumulative pluviometer. A film of paraffin preserved rain from any exchange with the atmosphere. As a consequence, most of rain samples during cyclonic periods correspond to a mix of several rain events. Over our period of 6 years, 678 rain samples have been collected, including 61 samples during cyclonic periods. The $\delta^{18}O_p$ and δD_p were analyzed by mass spectrometry (Finningan MAT 252) coupled with CO_2–H_2O equilibration and wavelength-scanned cavity ring down spectroscopy (Picarro) respectively. The accuracies on isotopic measurements are of ±0.05‰ and ±0.7‰ for $\delta^{18}O_p$ and δD_p respectively, leading to an average quadratic analytical uncertainty on deuterium excess (d_p) of ±0.8‰.

The Piton Maïdo meteorological station (21.077°S, 55.380°E, 2150 m a.s.l.), under the responsibility of Météo-France (the French national organization for meteorology), is the closest meteorological station from the Maïdo observatory (distance ~320 m). We use in this paper the hourly-cumulated precipitation data at this station ($P_{Maïdo}$ in mm/h).

2.2. Choice, Description and Representativeness of the Studied Low-Pressure Systems

The cyclonic season in the South-West Indian Ocean (from the equator to 40°S and from the eastern African coasts to 90°E) usually occurs during austral summer between November and April with a peak of activity from January to March. The cyclonic activity in this oceanic basin represented around 11% of the global cyclonic activity from 1999 to 2016 (Leroux et al., 2018; WMO, 2017). On average over this time period, 9.7 low-pressure systems per season developed, of which 9.4 were named when they strengthened to the moderate tropical storm stage and 4.8 reached the TC stage (Leroux et al., 2018).

The South-West Indian Ocean has been poorly observed and studied despite having tropical-system activity comparable to that of the North Atlantic Ocean with a significant modulation of cyclogenesis by large-scale conditions such as those associated with the Madden Julian Oscillation (Bessafi & Wheeler, 2006) and El Niño Southern Oscillation (Astier et al., 2015; Chang-Seng & Jury, 2010; Kuleshov et al., 2008, 2009). Moreover, this oceanic basin encompasses a number of vulnerable and poor islands and countries (Madagascar, Scattered Islands, Mozambique, Malawi). In addition, Réunion Island has recorded most of the world's maximum cumulative rainfall over time periods ranging from 12 hr to 15 days during cyclones (cyclone Gamede in 2007, Quetelard et al. (2009); cyclones Denise and Hyacinthe in 1966 and 1980 respectively, Holland (1993)).

The South-West Indian Ocean basin is monitored by the Regional Specialized Meteorological Centre (RSMC) at Météo-France in Réunion Island. The Direction Inter-Régionale de Météo-France pour l'Océan Indien (DIROI) of Météo-France also provides monthly meteorological bulletins (BCMOM) that summarize the weather situation on the Island and that detail the remarkable meteorological events for each month such as intense rainfalls.

The RSMC provides for each significant low-pressure system a comprehensive "best-track" dataset. The so-called "best-track" dataset consists of a postseason re-analysis of all the available observations to determine the best estimate of the system's position, intensity (Table 1), and other related parameters every 6 hr, over the entire lifetime of the system. More details on the "best-tracking" process can be found for example, in Knapp et al. (2010).

Between November 2014 and October 2020, 58 low-pressure systems were recorded and named in the South-West Indian Ocean basin by the RSMC. For some of these 58 systems, it can be difficult to clearly identify whether they had an impact on the observed rain events and on the isotopic composition of rain and water vapor at Réunion Island. For example, we observe that during some best-track periods Réunion Island can undergo large rain events fully disconnected from distant cyclonic live systems. We also observe that the isotopic composition of water vapor can be very depleted because of local atmospheric dynamics disconnected from distant cyclonic live systems. Thus, arbitrarily, we have first selected low-pressure systems that had over their best-track periods both a closest distance to Réunion Island smaller than 800 km (the center of the system is less than 800 km from the Maïdo site at some point during its lifetime) and a mean precipitation rate at Piton Maïdo higher than 5 mm/day. Fourteen of the 58 low-pressure systems satisfy these criteria (Table 2) and are identified for further study below.

We checked a posteriori that the common isotopic signal in water vapor exhibited for these selected systems, and described in Section 2.4, is not found during other systems that (a) traveled at a distance to Réunion Island between 800 and 1000 km (Fantala in 2016) or (b) traveled at a distance smaller than 800 km but with a mean precipitation rate lower than 5 mm/day (Cilida in December 2018, Francisco in February 2020, Herold in March 2020) or (c) gathered the two former conditions on minimum distance and minimum precipitation rate but that included precipitation events caused by local thunderstorms independent of the considered low-pressure systems according to Météo-France (Enawo in March 2017).

In order to examine the representativeness of the 2014–2020 period, we used precipitation data at Piton Maïdo station and cyclonic metrics on Réunion Island that are both available from the 1999 to 2000 cyclonic season. Since important gaps are found in the precipitation data for the 2001–2002, 2006–2007, and 2008–2009 cyclonic seasons, these three years are excluded from our analysis. Applying the same two criteria that were used to select the 14 low-pressure systems from 2014 to 2020, we observed that the number of cyclones per year varies between 0 and 6 (0 and 5 in our panel), that the number of best-track days varies between 0 and 66 days per year (0 and 48 in our panel), that the percentage of cyclonic rain over the year varies between 0% and 59% (0% and 74% in our panel) and last, that the cumulated annual precipitation at Piton Maïdo station varies between 662 and 1531 mm (671 and 2687 mm in our panel). The upper bound of 1531 mm is probably underestimated as the year 2006–2007 which included the cyclone Gamede, one of the wettest in the world (Quetelard et al., 2009), was not taken into

Table 2
Low-Pressure Systems Studied From 2014–2015 to 2019–2020 Cyclonic Seasons: Cyclonic Season, System Name, Best-Track Dates From RSMC Météo-France in dd/mm/yyyy, Cumulated Precipitation Over the Best-Track Periods From Météo-France Piton Maïdo Station, Minimal Distance of the System to Réunion Island, 10-Min Maximum Average Surface Wind

Cyclonic season	Name	Best-track start date (dd-mm-yyyy)	Best-track end date (dd-mm-yyyy)	$P_{\text{Maïdo}}$ (mm)	Minimal distance (km)	10 min-max wind (knot)
2014–2015	Bansi *	08/01/2015	19/01/2015	288.8	288	120
	Chedza	13/01/2015	22/01/2015	258.8	383	57
	Haliba	04/03/2015	13/03/2015	818.0	111	45
% Annual rain				74%		
2015–2016	Daya	07/02/2016	13/02/2016	181.2	397	38
% Annual rain				18%		
2016–2017	Carlos *	02/02/2017	15/02/2017	527.9	146	70
	Fernando	05/03/2017	16/03/2017	305.4	275	43
% Annual rain				58%		
2017–2018	Ava *	30/12/2017	09/01/2018	345.4	524	80
	Berguitta *	10/01/2018	24/01/2018	400.6	118	90
	Dumazile *	01/03/2018	10/03/2018	686.7	372	90
	Eliakim	13/03/2018	22/03/2018	222.0	561	60
	Fakir *	20/04/2018	26/04/2018	141.4	93	70
% Annual rain				72%		
2018–2019	–	–	–	–		
% Annual rain				0%		
2019–2020	Calvinia*	27/12/2019	03/01/2020	112.8	268	65
	Diane	22/01/2020	29/01/2020	47.9	215	40
	Esami	22/01/2020	26/01/2020	47.9	183	45
% Annual rain				35%		

Note: The contribution of cyclone-associated rain to annual rain (in %) is calculated from the isotopic pluviometer gauge at the Maïdo observatory from November to October as the Piton Maïdo Météo-France station had a gap in rainfall during 2 months in 2019. The stars indicate the systems that attained the stage of tropical cyclone (TC).

account. As a conclusion, our 6-year panel mostly covers the whole range of available recent observations. In addition, our panel includes two years with a high precipitation amount and a high proportion of cyclonic rain (2014–2015 and 2017–2018).

The 6-hr trajectory and intensity for the 14 systems extracted from the RSMC best-track dataset are shown on Figure 1. The 14 low-pressure depressions all formed northward of Réunion Island in the 5–20°S latitude band. The systems formed eastwards of Madagascar except two of them that developed in the Mozambique Channel: Diane and Chedza. We observe two major pathways for the 14 systems. Most of them had a parabolic-like pathway. The latter usually began in the North or North-East of Réunion Island at a latitude lower than 15°S and head toward the South-West. The tracks usually curved between 20° and 25°S and moved toward the South-East (Fakir, Ava, Eliakim, Dumazile, Berguitta, Daya, Carlos, Calvinia, Fernando, Haliba). In contrast, four systems exhibited a North-West to South-East trajectory (Esami, Bansi, Chedza, Diane) with a southwestward curve for Diane at around 25°S in its final stages. The latitude of Réunion Island is often close or slightly north to that at which cyclones usually completes their extra-tropical transition between 23° and 27°S (Bieli et al., 2019). The systems that passed closest to Réunion Island (distance to the system center inferior to 150 km) were Fakir, Haliba, Berguitta, Carlos and Esami (Table 2). The highest stage attained by those systems was the TC stage for Fakir. Only seven systems attained the TC stage and only Bansi attained the stage of Very Intense Tropical Cyclone (VITC) during a few hours at about 450 km from Réunion coasts (Figure 1). In 2015, Bansi and Chedza systems influenced Réunion Island over the same time periods (from January 8th to January 22nd). Similarly,

in 2020, Diane and Esami systems coexisted (from January 22nd to January 29th). In 2018, Ava and Berguitta systems followed each other (Table 2).

Due to frequent power cuts during cyclonic periods, two of the aforementioned low-pressure systems (Fernando in 2017 and Eliakim in 2018) were only partially sampled for water vapor ratios (less than 60% of hourly observations are available during the best-track periods). We thus exclude them from the processing of water vapor isotopic data.

We defined for each low-pressure system a "cyclonic period" that corresponds to the best-track period. The 10 days preceding and following the best-track periods serve as "reference periods". When these previous time periods overlapped between two systems (Bansi and Chedza, Berguitta and Ava, Diane and Esami), we excluded them from some analyses. The "number of best-track days" refers to the number of days tagged as "cyclonic period" during the studied period. The "number of low-pressure systems" refers to the number of low-pressure systems during the studied period. The "cyclonic rain" ("non-cyclonic rain") is the rain occurring during (outside) the best-track periods.

2.3. Classification of the Different Domains Within the Cyclone

Typical features are usually observed within tropical cyclones as the eye at the system center, surrounded by intense convective wall and spiral inner and outer rain bands reaching several hundreds of kilometers (Houze, 2010). For each of the 12 tropical cyclones for which water vapor isotopic ratios are available, we determined over the best-track time periods, and at the hourly scale, what kind of cyclonic substructure Réunion Island underwent. For this purpose, we use NCEP/CPC half-hourly globally merged 4-km resolution IR brightness temperature data merged from the European, Japanese, and U.S. geostationary satellites (GPM_MERGIR/V01) (Janowiak et al., 2017). The determination of a substructure is based on a closer visual examination of hourly maps of brightness temperature over a spatial domain centered on Réunion Island (7–37°S, 40–70°E) (see Figure S1 in Supporting Information) and on the calculation of average brightness temperature over Réunion Island. This large-scale view enables us to visually identify the position of the cyclone relative to Réunion Island, to determine the cyclonic structure impacting Réunion Island (system center, rain bands, environment between two rain bands) and to follow their time evolution. Brightness temperature varies from 165 to 330 K over the whole spatial domain. The lowest values (<210 K) correspond to high level clouds usually associated with intense convection whereas higher values are associated with lower convection in the rain bands (210–240 K) or lack of high and mid-level clouds (>280 K). The different cyclonic substructures (inner rain bands, outer rain bands, in between rain bands, intense convective regions) are identified as follows (see Figure S1 in Supporting Information for some examples):

- None of the 12 studied cyclones exhibited eye and eye-wall regions over Réunion Island visible on the maps. However, some systems approached Réunion Island closely and the strong convective region around the system center is visible and sometimes encompassed Réunion Island. This domain exhibits very low brightness temperature. It is identified when the averaged brightness temperature over Réunion Island is lower than the arbitrary threshold of 215 K (and tagged as C domain; Figure S1a in Supporting Information). This substructure was identified for three low-pressure systems (Carlos, Berguitta, Fakir) during the days when the system centers were closest to Réunion Island. The lifetime of this substructure over Réunion Island never exceeds a few hours.
- Beyond the system center, the inner rain band domain (tagged as IB) is defined as the first encountered spiraled rain band originating from the system center (Houze, 2010) and encompassing Réunion Island. The brightness temperature never exceeds 260 K in the inner rain band. For some of the studied cyclones (Ava, Bansi, Chedza, Daya, Calvinia) we did not capture this substructure over Réunion Island.
- The more distant spiraled outer rain bands impacting Réunion Island are visually identified (and named OB; Figure S1b in Supporting Information). As for IB, brightness temperature is lower than 260 K. The first and the last outer bands at the edge of the system affecting Réunion Island, potentially affected by the environment outside the cyclone, are identified (and tagged as FOB and LOB respectively; Figure S1c in Supporting Information). The OB substructure has been identified for each system except for Esami.
- When the averaged brightness temperature over Réunion Island is lower than 220 K inside an inner (IB) and an outer (OB) rain band, we identified them (and named them as IBC and OBC respectively to indicate more intense convection; Figure S1d in Supporting Information). In addition, for some identified rain bands, no

precipitation was observed at the Maïdo observatory. To differentiate rainy and non-rainy bands, each of the aforementioned rain bands substructure is tagged as rainy if $P_{\text{Maïdo}}$ is higher than 1 mm/hr.

- Last, the region encompassed between two spiraled bands (IRB; Figure S1e in Supporting Information) corresponds to averaged brightness temperature exceeding 260 K.

With this classification, the Esami system developed none of the aforementioned substructures over Réunion Island as it moved away from Réunion Island right after its genesis (Figure 1).

2.4. The Global Precipitation Measurement (GPM) Data

We use the classification proposed by the Global Precipitation Measurement Dual-frequency Precipitation Radar (GPM-DPR) 2ADPR/V07 product (Iguchi & Meneghini, 2021) to identify the proportion of stratiform and shallow rain over a domain centered on Réunion Island and of size 6° × 6° (18.125°S–24.125°S and 52.5°–58.5°S). We had to consider a large area around Réunion Island to have sufficient data per year (between 33% and 60%) because of the limited satellite GPM mission coverage.

2.5. Isotope-Enabled Atmospheric General Circulation Models

In order to gain insight into the processes that control the isotopic composition of rain and water vapor within tropical cyclones, we use in this paper daily outputs (precipitation and isotopic ratios) from two isotope-enabled AGCMs that are among the most recent AGCMs offering simulations nudged to ERA5 reanalysis (Hersbach et al., 2020) over our studied period.

First, the LMDZ-iso model (Risi et al., 2010) is the isotopic version of the AGCM LMDZ6A (Hourdin et al., 2020), with a spatial resolution of 1.875° in latitude and 3.75° in longitude and 79 vertical levels. The 3D-fields of horizontal winds are relaxed at each time step toward those of the ERA5 reanalysis (Hersbach et al., 2020) with a relaxation time scale of 3 hr, following the method of Coindreau et al. (2007). The sea surface temperature (SST) and sea ice fields from AMIP (Atmospheric Model Intercomparison project) have been applied (Gates et al., 1999). The sea water isotopic composition is uniform and sets to +0.5‰ for $\delta^{18}O$ and 0‰ for deuterium excess. The grid cell that includes Réunion Island (and is used to compare with observations there) is centered on 21.78947°S and 56.25°E with 5.1% of land fraction.

Second, ECHAM6-wiso (Cauquoin et al., 2019; Cauquoin & Werner, 2021) is the isotopic version of the AGCM ECHAM6 (Stevens et al., 2013). The implementation of the water isotopes in ECHAM6 has been described in detail by Cauquoin et al. (2019), and has been updated and evaluated in several aspects by Cauquoin and Werner (2021). We used two simulations at T127L95 and T63L47 spatial resolution (0.9° horizontal resolution and 95 vertical levels and 1.9° horizontal resolution and 47 vertical levels respectively) nudged to ERA5 reanalysis (Hersbach et al., 2020). The ECHAM6-wiso 3D-fields of temperature, vorticity and divergence as well as the surface pressure field are relaxed at each time step toward those of the reanalysis data with a relaxation time scales ranging from 6 to 48 hr. Although the nudging protocol is similar between LMDZ-iso and ECHAM6-wiso, the nudging is stricter in LMDZ-iso (shorter relaxation time scales), but the nudging of the vorticity in ECHAM6-wiso is expected to favor a more faithful simulation of tropical depressions and cyclones. The SST and sea ice fields from the ERA5 reanalysis have been applied as ocean surface boundary conditions. The sea water $\delta^{18}O$ is from the global gridded data set of LeGrande and Schmidt (2006) and deuterium excess is set to 0‰. For the T127L95 spatial resolution, the grid cell including Réunion Island is centered at 21.04°S and 55.3125°E with 20% of land fraction. For the T63L47 spatial resolution, the closest grid cell of Réunion Island is centered at 21.45°S and 56.25°E. This cell and the surrounding area are purely oceanic in this configuration.

3. What Does the Isotopic Composition of Precipitation Record?

3.1. Relationship Between $\delta^{18}O_p$, Number and Duration of Low-Pressure Systems and Proportion of Cyclonic Rain

Precipitation amount delivered at the Piton Maïdo station during the 14 identified low-pressure systems varied from 47.9 to 818.0 mm over the best-track periods. The contribution of cyclone-associated precipitation to annual precipitation varied from 18% to 74% depending on the year (Table 2). This annual contribution is correlated to (a) the number of best-track days per year that can be a tracer of cumulated duration of low-pressure systems impacting Réunion Island: the larger the number of cyclones, the larger the number of best-track days, the

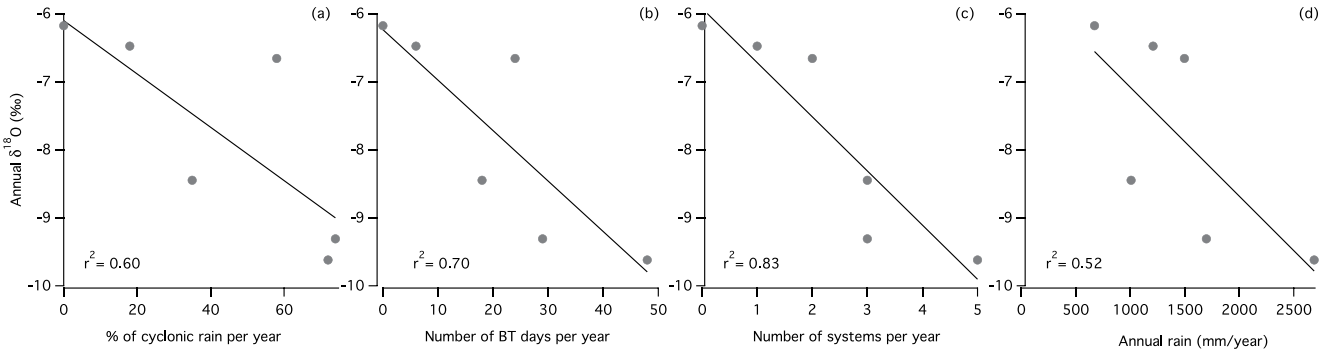

Figure 2. Annual mean amount-weighted $\delta^{18}O_p$ as a function of (a) the percentage of cyclonic rain per year; (b) the number of best-track days per year; (c) the number of low-pressure systems per year; (d) the cumulated annual precipitation.

larger the contribution of cyclonic rain ($r^2 = 0.90$, $n = 6$, $p < 0.01$), and (b) to a lesser extent to the number of low-pressure systems per year: more cyclones lead to more cyclonic rain ($r^2 = 0.63$, $n = 6$, $p < 0.1$).

The annual mean amount-weighted $\delta^{18}O_p$ ($\delta^{18}O_{p\_all\ rain}$) from 2014 to 2020 varies from −6.18‰ (2018–2019) to −9.62‰ (2017–2018). Without accounting for cyclonic rains (Section 2), the annual mean amount-weighted $\delta^{18}O_p$ ($\delta^{18}O_{p\_without\ cyclonic\ rain}$) from 2014 to 2020 is always higher than $\delta^{18}O_{p\_all\ rain}$. The difference is directly proportional to the percentage of cyclonic rain per year ($r^2 = 0.96$, $n = 6$, $p < 0.001$) and increases of 0.5‰ per a 10%-increase in the cyclonic rain proportion. The covariance of $\delta^{18}O_{p\_all\ rain}$ with the percentage of cyclonic rain is of $r^2 = 0.60$ ($n = 6$, $p < 0.1$), and increases to $r^2 = 0.70$ ($n = 6$, $p < 0.01$) and $r^2 = 0.83$ ($n = 6$, $p < 0.05$) with the number of best-track days and with the number of low-pressure systems per year respectively (Figure 2).

The annual mean $\delta^{18}O_v$ from 2014 to 2020 shows a low inter-annual variability from −14.5% to −16.5‰ with no relationship to the percentage of cyclonic rain or to the number of best-track days or to the number of low-pressure systems. However, as expected above, when considering the annual mean $\delta^{18}O_v$ only for rainy days ($P_{Maïdo} > 5$ mm/d), significant correlation appears with the number of low-pressure events ($r^2 = 0.62$, $n = 6$, $p < 0.001$), with the number of best-track days ($r^2 = 0.35$, $n = 6$, $p < 0.001$) and to a lesser extent with the proportion of cyclonic rain ($r^2 = 0.23$, $n = 6$, $p < 0.001$). These correlations do not increase significantly when increasing the $P_{Maïdo}$ threshold above 5 mm/d.

We further analyze below how the annual isotopic signal results from seasonal $\delta^{18}O$ variations.

The isotopic composition of precipitation exhibits a clear mean seasonal cycle over 2014–2020 (Figure 3) with isotopic depleted values during the rainy season, from December to April (mean $\delta^{18}O_p = -8.5 \pm 1.1$‰) and enriched values by 4‰ during the non-rainy season, from May to November (mean $\delta^{18}O_p = -4.5 \pm 0.5$‰). The mean amount-weighted $\delta^{18}O_p$ over the rainy season over 2014–2020 without accounting for cyclonic rains is −6.4 ± 0.7‰. Thus, cyclonic rains explain around half (2.1‰) of the isotopic variation between the rainy and the non-rainy season. The inter-annual spread of monthly $\delta^{18}O_p$ and precipitation is more important during the rainy season than during the non-rainy season. It clearly depends on the presence or absence of cyclonic rains and of the amount of rain during the rainy season (see the ±1σ on Figure 3). Indeed, the highest (lowest) mean $\delta^{18}O_p$ over the rainy season is recorded for 2018–2019 (2017–2018) at −6.9‰ (−10.1‰) with a minimum (maximum) in precipitation of 415.5 mm (2460.6 mm) when no cyclone (4 cyclones) impacted the Island. The mean amount-weighted $\delta^{18}O_p$ over the rainy season is significantly related to the proportion of cyclonic rain during this period ($r^2 = 0.90$, $n = 6$, $p < 0.01$), to the number of low-pressure systems during this period ($r^2 = 0.77$, $n = 6$, $p < 0.01$) and to the number of best-track days during this period ($r^2 = 0.56$, $n = 6$, $p < 0.01$). When removing the cyclonic rains from the mean amount-weighted $\delta^{18}O_p$ over the rainy season, previous correlations fall down to $r^2 = 0.1$.

In contrast to $\delta^{18}O_p$, it is worth noting that the isotopic composition of water vapor does not exhibit seasonal variations: mean $\delta^{18}O_v$ from December to April (May to November) is −15.3 ± 0.8‰ (−15.4 ± 0.7‰) (Figure 3). The seasonal variation of $\delta^{18}O_v$ is still missing when separating rainy days ($P_{Maïdo} \geq 0.2$ mm/d) from the others ($P_{Maïdo} = 0$ mm/d): mean $\delta^{18}O_v$ from December to April (May to November) is −15.4 ± 1.0‰ (−14.8 ± 0.8‰) (Figure 3). A depletion of mean $\delta^{18}O_v$ appears from December to April ($\delta^{18}O_v = -16.6 \pm 1.0$‰) compared to May to November ($\delta^{18}O_v = -14.8 \pm 0.7$‰) when considering only

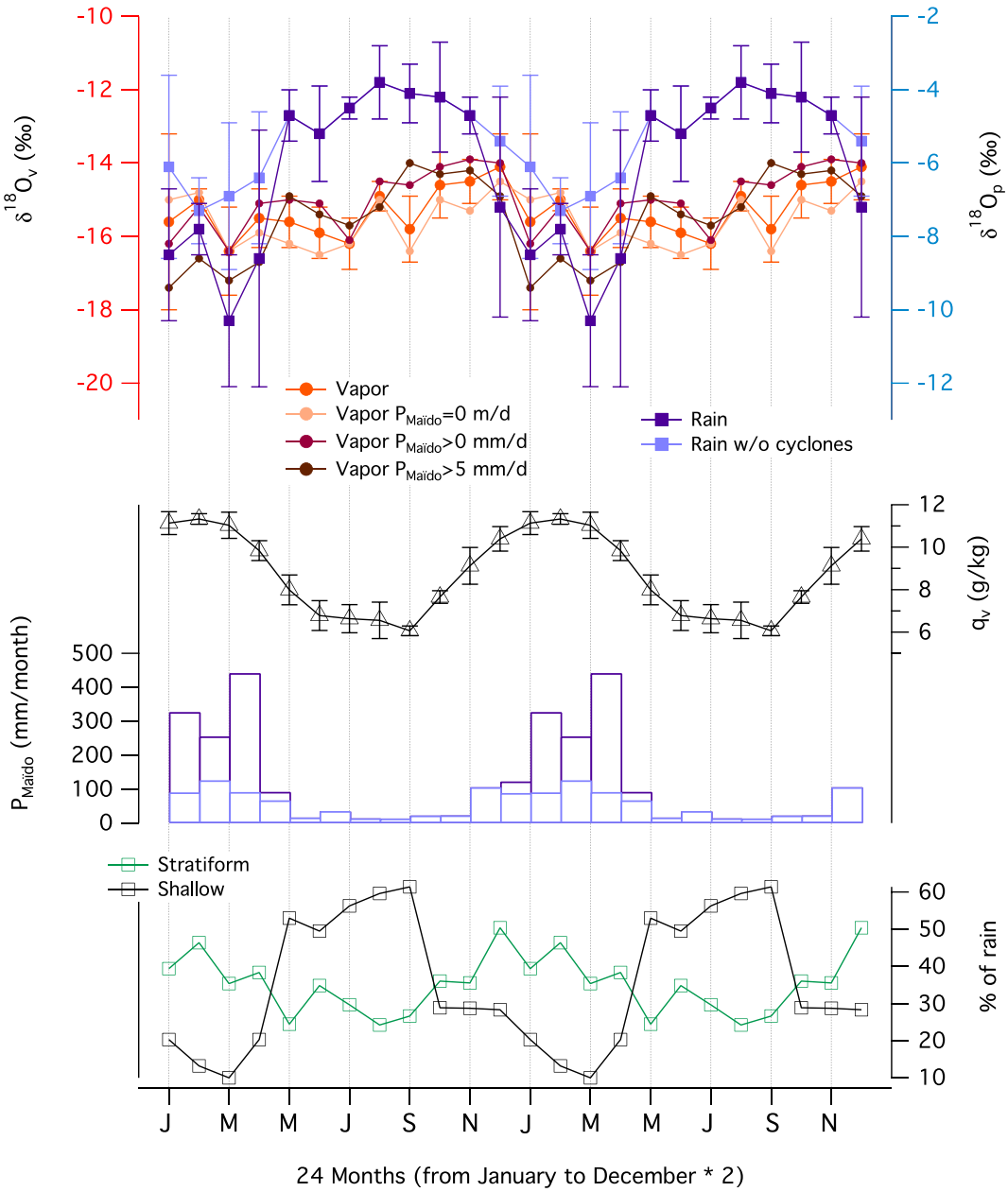

Figure 3. Mean seasonal cycle of different variables calculated over 6 years (2014–2020). For ease of reading, the mean seasonal cycle is duplicated two times to show clearly the dry-wet-dry season transition. From top to bottom: $\delta^{18}O_v$ (‰) for different precipitation rates at the Maïdo station ($P_{Maïdo} = 0$ mm/d, $P_{Maïdo} > 0$ mm/d, and $P_{Maïdo} > 5$ mm/d) and $\delta^{18}O_p$ (‰) with and without cyclonic periods; water vapor mixing ratio q_v (g/kg); average precipitation at the Piton Maïdo meteorological station (mm/month) with cyclonic rain (i.e., all rain) and without cyclonic rain with the same code color than for $\delta^{18}O_p$; percentage of stratiform and shallow precipitation from GPM (Global Precipitation Measurement) over a domain of 6° × 6° centered on Réunion Island.

rainy days with $P_{Maïdo} > 5$ mm/d. The lack of seasonal variations in $\delta^{18}O_v$ could be due to two competing effects: depleted isotopic values are found both from December to April due to cyclonic and intense rain events and from May to October due to nighttime large-scale subsidences at the Maïdo site, leading also to much drier conditions than during cyclonic events (Guilpart et al., 2017). This explains why the proportion of cyclonic rain and the number, and the duration of low-pressure systems have an influence on $\delta^{18}O_v$ only for rainy days at the inter-annual timescale.

According to these observations, a robust relationship exists between the annual isotopic composition of precipitation, the proportion of cyclonic rain over the year and the number and the duration of low-pressure systems per year. Obviously, these latter three parameters are not independent as mentioned above. The annual mean $\delta^{18}O_p$ thus appears as a correct candidate to reconstruct quantitatively past frequency of tropical cyclones from annual archives of isotopic composition of rain.

These relationships between $\delta^{18}O_p$ and cyclone activity are likely linked to annual precipitation amount as the latter is strongly correlated to the number of cyclones ($r^2 = 0.74$, $n = 6$). Previous studies have indeed suggested that relationships between annual $\delta^{18}O_p$ and low-pressure systems frequency are caused by a stronger isotopic depletion when rain originates from mature mesoscale convective systems that form in organized and persistent convective systems (Kurita, 2013; Risi et al., 2021). In the next section, we examine from our dataset whether, and to which extent, the amount effect, that is, the decrease of $\delta^{18}O_p$ as precipitation rate increases (Dansgaard, 1964), is different for cyclonic and non-cyclonic rains.

3.2. Amount Effect

A negative relationship is observed between annual mean $\delta^{18}O_p$ and cumulated annual rain ($r^2 = 0.52$, $n = 6$, $p < 0.1$) (Figure 2). This relationship is expected from the above results as the annual precipitation varies with the number of low-pressure systems per year. This correlation increases up to $r^2 = 0.70$ ($n = 5$, no low-pressure system in 2018–2019) when considering the difference $\delta^{18}O_{p\_all\ rain} - \delta^{18}O_{p\_without\ cyclonic\ rain}$ as a function of cumulated precipitation over the best-track periods, and falls to $r^2 = 0.12$ when cyclonic rains are excluded. This correlation is thus mainly driven by cyclonic rains suggesting that atmospheric processes within or in the vicinity of cyclones deplete the rain more efficiently than in less organized system.

One of the main features of cyclonic rain is the presence of stratiform rain around convective bands as organized low-pressure systems such as tropical cyclones develop large stratiform regions (Yang et al., 2018). Annual stratiform rain fraction, from GPM data set, increases with annual total precipitation ($r^2 = 0.58$, $n = 6$, $p < 0.1$) and a significant negative relationship is seen between annual $\delta^{18}O_p$ and the percentage of stratiform rain $r^2 = 0.58$ ($n = 6$, $p < 0.1$). This is consistent with Aggarwal et al. (2016) and independent of the cyclonic or non-cyclonic character of precipitation.

At the seasonal scale, the covariance between $\delta^{18}O_p$ and $P_{Maïdo}$ is of $r^2 = 0.77$ ($n = 12$, $p < 0.001$) and decreases to $r^2 = 0.61$ ($p < 0.01$) without cyclonic rain. The $\delta^{18}O_p$ seasonal cycle is well anti correlated with the fraction of stratiform precipitation ($r^2 = 0.41$) (Figure 3). The latter varies between 40% and 60% from November to April, twice higher than outside the cyclonic season. Interestingly, the (positive) correlation between the $\delta^{18}O_p$ seasonal cycle and the fraction of shallow precipitation, from GPM data set, is higher ($r^2 = 0.64$, $n = 12$, $p < 0.001$), consistent with a high sensitivity of $\delta^{18}O_p$ to the large-scale ascent profile (Lacour et al., 2018; Risi et al., 2020; Torri et al., 2017) (Figure 3). At the monthly scale, the correlation between $\delta^{18}O_p$ and the proportion of stratiform precipitation hold true ($r^2 = 0.22$, $n = 72$, $p < 0.001$) and increases up to $r^2 = 0.88$ ($n = 8$, $p < 0.001$) when calculated from average $\delta^{18}O_p$ over intervals of 10%-stratiform precipitation proportion (from 0.25% to 75%). However, $\delta^{18}O_p$, $P_{Maïdo}$ and the proportion of stratiform rain all exhibit a strong seasonal cycle (certainly explaining the magnitude of the covariance) and it is necessary to examine the amount effect at the synoptic scale.

Figure 4a shows the relationship between $\delta^{18}O_p$ and amount of rain per rain sample for cyclonic and non-cyclonic rains. We observe that during cyclonic (non-cyclonic) periods, $\delta^{18}O_p$ varied between −15.15‰ and −2.13‰ (between −12.81 and 3.55‰) and the mean amount-weighted $\delta^{18}O_p$ is −10.28 ± 1.95‰ (−5.90 ± 2.29‰). On average, the slope of the amount effect for cyclonic and non-cyclonic rain is not different at the 67% confidence level (±1σ) (−0.022 ± 0.04‰/mm vs. −0.018 ± 0.001‰/mm). However, we observe a stronger isotopic depletion for cyclonic rain by −1.6 ± 0.4‰ ($n = 3$) (Figure 4a). At the daily scale, average $\delta^{18}O_p$ over intervals of 10%-stratiform precipitation proportion (from 0% to 94%) clearly decreases with the stratiform character of precipitation ($r^2 = 0.45$, $n = 11$, $p < 0.001$) (for each day in which a stratiform fraction is given in the GPM data set, we have assigned it the $\delta^{18}O_p$ of the rain sample including that day if such an event exists).

Our results suggest that processes that deplete the rain in stratiform regions of low-pressure systems, such as the water–vapor interactions (Kurita, 2013; Risi et al., 2008, 2021), contribute to the amount effect. Actually, these relationships between $\delta^{18}O_p$ and precipitation are intimately related to the so-called "vapor amount effect" as mentioned by Risi et al. (2020, 2021). We observe that at both hourly and daily scales, $\delta^{18}O_v$ and $P_{Maïdo}$ are anti-correlated with on average a stronger depletion during cyclonic periods by −5.5 ± 1.4‰ ($n = 7$) and

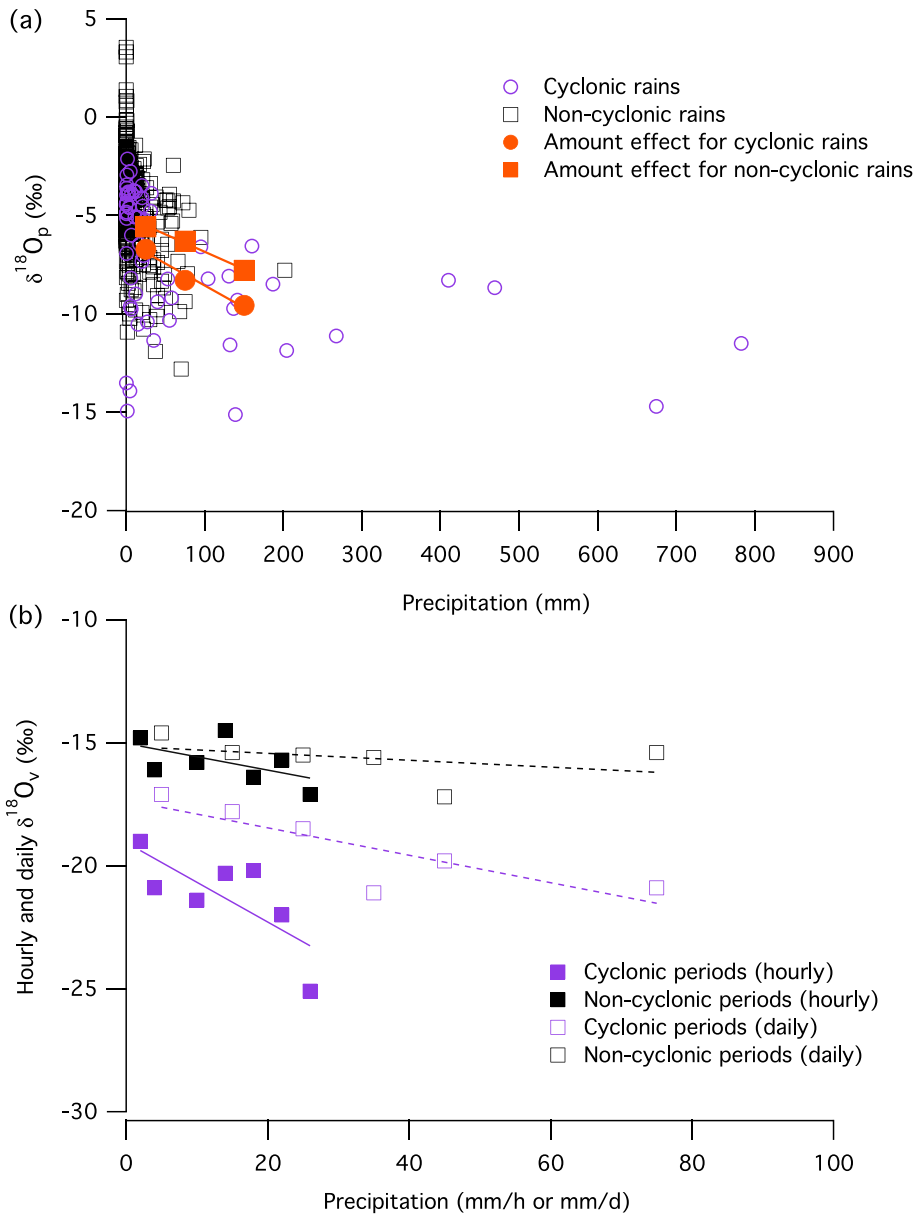

Figure 4. (a) Isotopic composition ($\delta^{18}O_p$ in ‰) of all rain samples as a function of precipitation amount (mm) (purple open circles are for rain occurring during cyclones and black open squares are for rain occurring outside cyclones). Orange circles (squares) are amount-weighted mean $\delta^{18}O_p$ during (outside) cyclonic periods for three different precipitation intervals common to cyclonic and non-cyclonic periods; (b) Hourly and daily isotopic composition of water vapor ($\delta^{18}O_v$ in ‰) as a function of precipitation rate (mm/h and mm/d respectively) at the Piton Maïdo station for cyclonic (purple) and non-cyclonic (black) time periods. Each marker is the average of hourly or daily $\delta^{18}O_v$ over a precipitation rate interval of 4 mm/hr and 10 mm/d respectively.

-3.6 ± 1.5‰ ($n = 6$) respectively (Figure 4b). A steeper amount effect (i.e., a more negative $\delta^{18}O/P$ slope) is also observed for cyclonic periods at the 67% confidence level ($\pm 1\sigma$) both at the hourly (-0.161 ± 0.063‰/mm/h vs. -0.055 ± 0.037‰/mm/h) and at the daily scale (-0.056 ± 0.018‰/mm vs. -0.014 ± 0.016‰/mm) relative to non-cyclonic periods (Figure 4b).

3.3. Summary

Our observations show that annual $\delta^{18}O_p$ strongly depends on the proportion of cyclonic rain, the duration and the number of low-pressure systems per year. This correlation likely reflects a systematically stronger depletion

during low-pressure systems: even for a given precipitation rate, mean amount-weighted $\delta^{18}O_p$ is lower in cyclonic rain than in non-cyclonic rain by 1.5–2‰. This could be related to the higher proportion of stratiform rain within cyclones. The water vapor also exhibits a systematically stronger depletion during cyclonic periods and, in addition, a steeper amount effect during cyclonic periods with a $\delta^{18}O_p/P$ slope 3–4 times higher. The depleted isotopic ratio in rain during tropical cyclones is thus intimately related to the influence of cyclones on the water vapor isotopic ratio and to interaction between both phases as already suggested by Risi et al. (2020, 2021, 2023).

Previous studies concluded that multiple processes act together to deplete the isotopic composition of both water vapor and rain within mesoscale convective systems when precipitation increases: the increased efficiency of updraft and downdraft to export respectively enriched and depleted water vapor from and toward the surface layer (Kurita, 2013; Risi et al., 2008, 2021), the decreased rate of snow sublimation above the melting level increasing the quantity of snow precipitation which depletes the rain at lower altitude (Risi et al., 2021), the decreased fraction of evaporated rain drop in humid conditions inducing a more depleted evaporative flux toward the surrounding water vapor (Risi et al., 2008, 2020, 2021; Tremoy et al., 2014), the larger flux of evaporated precipitation when precipitation increases (even if the fraction of evaporated rain decreases) which has a depleted effect on the surrounding water vapor (Field et al., 2010; Worden et al., 2007), and the increase of diffusive exchanges between depleted rain that forms at higher altitude than water vapor in which its falls (Lawrence et al., 2004; Lee & Fung, 2008) inducing the isotopic depletion of the sub-cloud layer and of subsequent rain.

In the next sections, we explore whether daily to hourly $\delta^{18}O_v$ observations can help in detecting and discussing the role of such enhanced processes in depleting both water vapor and rain in the vicinity of low-pressure systems.

4. How Do Cyclones Impact Water Vapor Isotopic Ratio at the Synoptic Scale?

4.1. V-Shaped Variations in $\delta^{18}O_v$ at the Synoptic Scale

The common feature of $\delta^{18}O_v$ within the best-track periods is a pronounced isotopic depletion over several days following a V-shape as already observed by Bhattacharya et al. (2022) (Figures 5 and 6). This V-shaped pattern is not always observed for tropical cyclones, as reported for example, by Wang et al. (2021). Considering the 12 systems, the daily isotopic minimum during the V-shaped variation ranged from −21.0‰ (Ava) to −29.8‰ (Fakir). It is worth noting that other time periods outside best-track periods exhibit very low daily $\delta^{18}O_v$ with a V-shaped variation for some of them. They mostly correspond either to time periods without rain exhibiting several consecutive very isotopic depleted nights as explained in Guilpart et al. (2017) (see black arrows in Figures 5 and 6) or to intense rainfall driven by the regional-scale circulation as convective detrainment from Madagascar or southern arrival of a cold front as described by Météo-France in their BCMOM (see blue arrows in Figures 5 and 6). It is worth noting that in contrast to $\delta^{18}O_v$, there is no specific change either in d_v or in q_v during cyclonic periods. Mean d_v is similar over the 10 days preceding the best-track period, over the best-track periods, and over the 10 days following (12.1 ± 1.2‰, 12.8 ± 2.1‰, and 12.4 ± 2.3‰ respectively, $n = 12$ for best-track periods and $n = 10$ for the reference periods). The mean water mixing ratio during the 12 best-track periods is equal or higher (lower) than during 10 days before for 9 (3) systems by +1.4 ± 1.1 (−1.1 ± 0.9) g/kg. Average q_v over the 10-days periods after the best-track is always equal or lower than over the best-track periods by −1.8 ± 1.1 g/kg.

Owing to the hourly $\delta^{18}O_v$ data (see Section 5.1), we can describe below in details how the V-shaped pattern is formed.

For some systems (Bansi, Daya, Diane and Esami), the start of the isotopic fall precedes the best-track period by a few hours up to more than 1 day (Figures 5 and 6 and Figure S2 in Supporting Information). For Bansi, the early fall is probably related to its close genesis 300 km northwestward of Réunion Island. For Daya, a convective cloud roll from a large monsoon flux is located eastwards, halfway between Réunion Island and Tromelin Island (15.87°S, 54.42°E). The rain bands linked to this initial low-pressure system reached Réunion Island from 5 February 2016 (i.e., 2 days before the best-track period) (according to the BCMOM for February 2016). The early fall is thus explained by the presence of storm instability in the area before the RCSM monitoring of the system. The early isotopic depletion can also be explained by intense local rain disconnected from the considered low-pressure system. This is well illustrated by the sharp isotopic depletion of ∼15‰ occurring around 30 hr before the start of the Diane and Esami best-track periods on January 22nd. This isotopic fall is most likely caused by an important rain event between 18:30 UTC on January 20th and 09:30 UTC on January 21st, with a cumulated precipitation of 68.2 mm (according to the BCMOM for January 2020). Deep convection took place

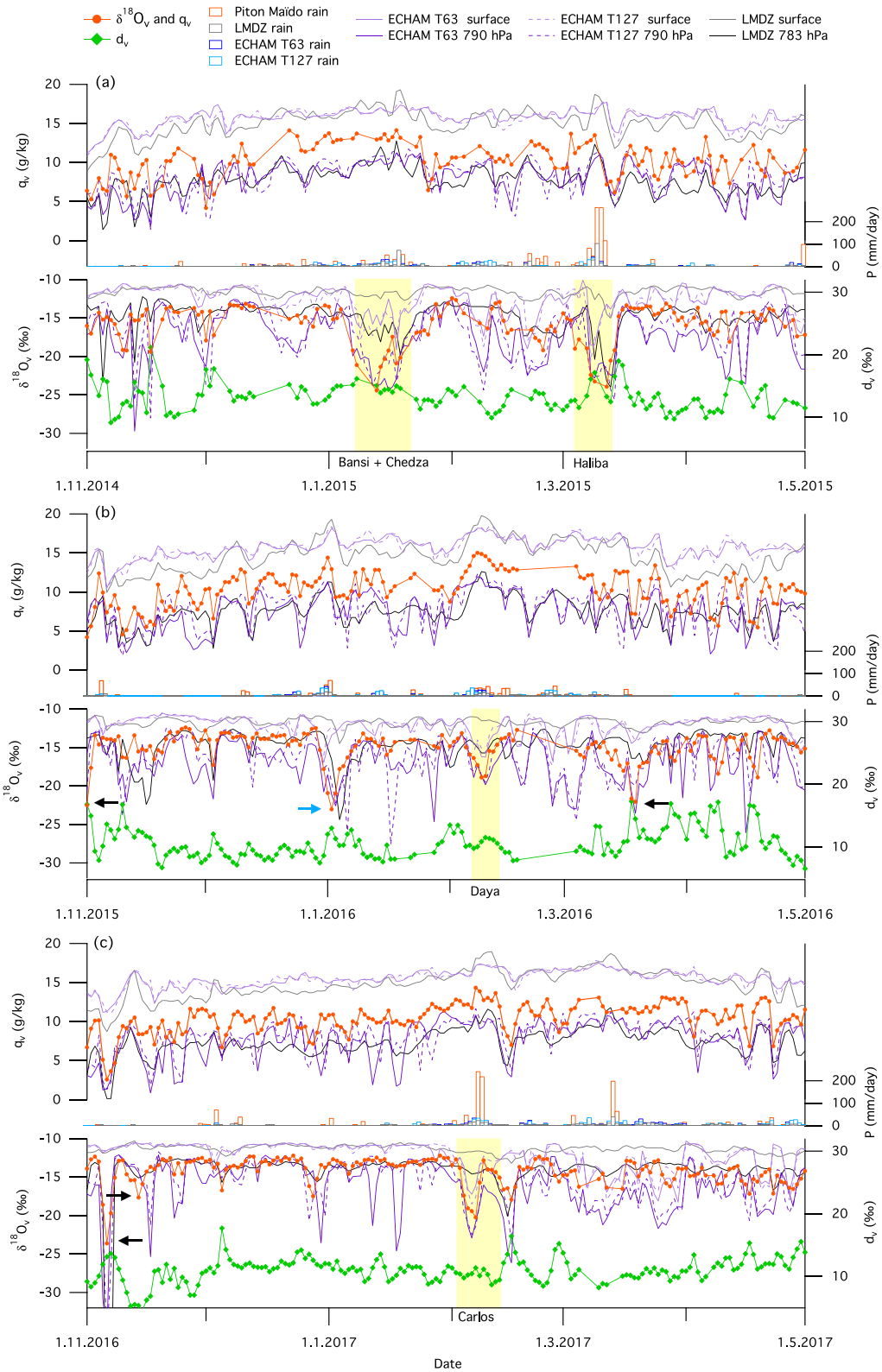

Figure 5.

during a few hours over Réunion Island: the mean outgoing longwave radiation over the whole island decreases to 144 $W \cdot m^{-2}$ and the mean vertical velocity at 500 hPa exhibited a fall down to -1.3 Pa $\cdot s^{-1}$, a value that can be associated with extreme precipitation in this region (see for example Li & O'Gorman, 2020). This rain event is due to the arrival of an intense large-scale rainy front from the South-West and it is thus disconnected from the minimal pressure systems precursor of Esami and Diane located east of the island and in the Mozambique Channel respectively at these dates. At last, the $\delta^{18}O_v$ depletion during the best-track periods is probably caused by Diane that went by the island after Esami.

In contrast, for some other systems, $\delta^{18}O_v$ keeps a constant mean level at the beginning of the best-tracks periods during a few days. This is well illustrated for Carlos and Ava that formed far from Réunion Island and did not affect the water isotopic composition at the beginning of the best-track period.

The $\delta^{18}O_v$ generally starts to increase before the end of the best-track period. Some systems retrieve (sometimes very quickly, in a few hours) a stable $\delta^{18}O_v$ mean level 1–5 days before the end of the best-track period (Berguitta, Dumazile, Diane) (Figure S2 in Supporting Information). After the best-track period, for some systems, $\delta^{18}O_v$ keeps increasing a few hours (Haliba) to a few days (Chedza, Fakir, Calvinia) before reaching again a stable mean $\delta^{18}O_v$ value comparable to the mean $\delta^{18}O_v$ of the days before the best-track (the 10-day periods before and after the best-track generally exhibit a similar average $\delta^{18}O_v$ of -15.7 ± 1.3‰ and -15.5 ± 2.0‰ respectively ($n = 10$)).

Our observations are in line with the mechanism proposed by Bhattacharya et al. (2022) on the possible factors controlling the formation of the V-shaped $\delta^{18}O_v$ pattern. Using an idealized model based on Rayleigh fractionation and on moisture mixing, they proposed that the rapid and abrupt $\delta^{18}O_v$ fall in the left limb of the V-shaped pattern is produced by a continuous heavy rainout along the cyclone pathway with a constant mass of moving water vapor, supplied by both continuous import of moisture from low-level and from oceanic evaporation, that continuously depletes. The slow recovery of the stable $\delta^{18}O_v$ mean level, forming the right limb of the V-shaped, is due to the water vapor being progressively replaced by the ambient oceanic vapor.

4.2. Comparison of Daily Observations With ECHAM6-Wiso and LMDZ-Iso Outputs

Both ECHAM6-wiso and LMDZ-iso models fail to reproduce the V-shaped isotopic variability at the surface level during the best-track periods (Figures 5 and 6). However, the V-shaped pattern is captured at the 790 hPa vertical level that corresponds to the altitude of the Maïdo Observatory (the coarse resolution of our simulations does not capture the topography of Réunion Island). While ECHAM6-wiso well reproduces the amplitude of the isotopic depletion at 790 hPa for most of the low-pressure systems and at both spatial resolution (T63 and T127), LMDZ-iso mostly underestimates this isotopic depletion (Figures 5 and 6) except for three cyclones (Haliba, Dumazile and Fakir) and it is necessary to seek for a higher level (up to 640 hPa, not shown) to find the measured isotopic depletion. The fact that the two AGCMs, at such a medium to coarse resolution, are able to capture the observed variations, without explicit representation of the island or of convective motions, suggests that the V-shaped isotopic depletion during the best-track periods at the Maïdo observatory site is driven by large-scale processes and thus representative of the large-scale.

In detail, ECHAM6-wiso captures the amount effect for both water phases and displays a stronger $\delta^{18}O$ depletion of precipitation and water vapor for cyclonic rains at a given precipitation rate, consistent with observations, by -1.2 ± 0.4‰ at the surface level for both phases and both spatial resolutions (Figure 7), and by -2.5 ± 0.8‰ at 790 hPa for water vapor and for both spatial resolutions. The $\delta^{18}O/P$ slopes for cyclonic and non-cyclonic periods are not significantly different at the 67% confidence level for both phases (Figure 7). Therefore, the stronger local precipitation during cyclones is not sufficient to explain why the model simulates a stronger depletion in case of cyclones since even for the same local precipitation cyclonic rains are more depleted. We may hypothesize that during tropical cyclones, the precipitation is stronger over a larger region and over a longer period of time. Since water vapor isotopes integrate processes temporally and spatially along trajectories (Bhattacharya et al., 2022;

Figure 5. (a) Daily water vapor mixing ratio (q_v in g/kg), daily precipitation (mm/d), daily isotopic composition of water vapor ($\delta^{18}O_v$ in ‰) from observations at the Maïdo site and from LMDZ-iso and ECHAM6-wiso models at the surface level and at the Maïso site level (i.e., the 783 hPa level in LMDZ-iso and the 790 hPa level in ECHAM6-wiso) over the rainy season 2014–2015 (from 1 November 2014 to 1 May 2015, with the format day/month/year). Daily deuterium excess of water vapor (d_v in ‰) from observations at the Maïdo site is in green. The best-track periods of the studied low-pressures are shown in yellow or orange; (b) same than (a) for 2015–2016; (c) same than (a) for 2016–2017. Black arrows are some examples of V-shaped daily $\delta^{18}O_v$ due to consecutive very depleted nights. Blue arrows are some examples of V-shaped $\delta^{18}O_v$ due to intense rainfall outside the best-track periods.

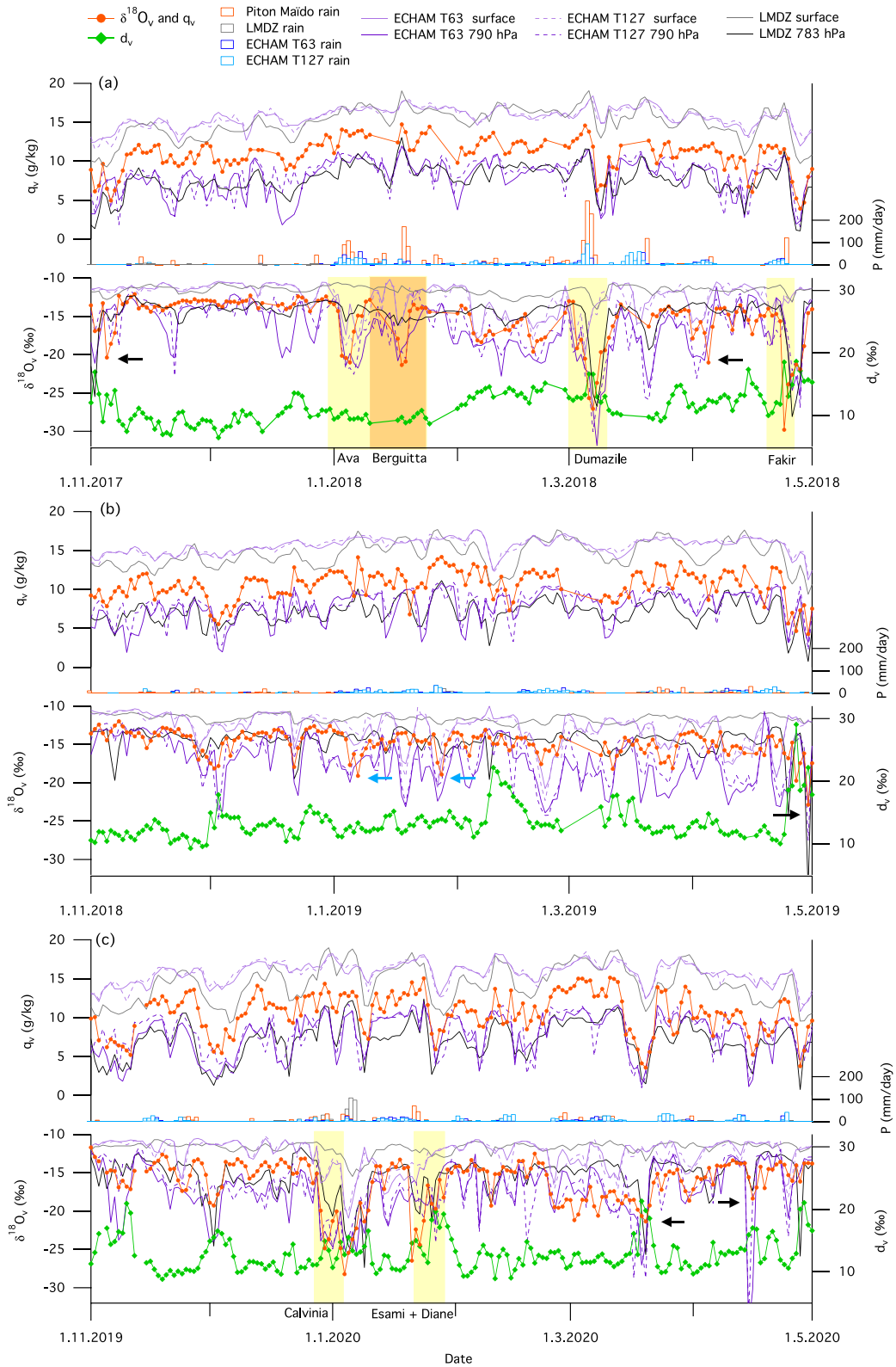

Figure 6. Same as Figure 5 for (a) for 2017–2018; (b) 2018–2019 (no Piton Maïdo rain data over January and February 2019); (c) for 2019–2020.

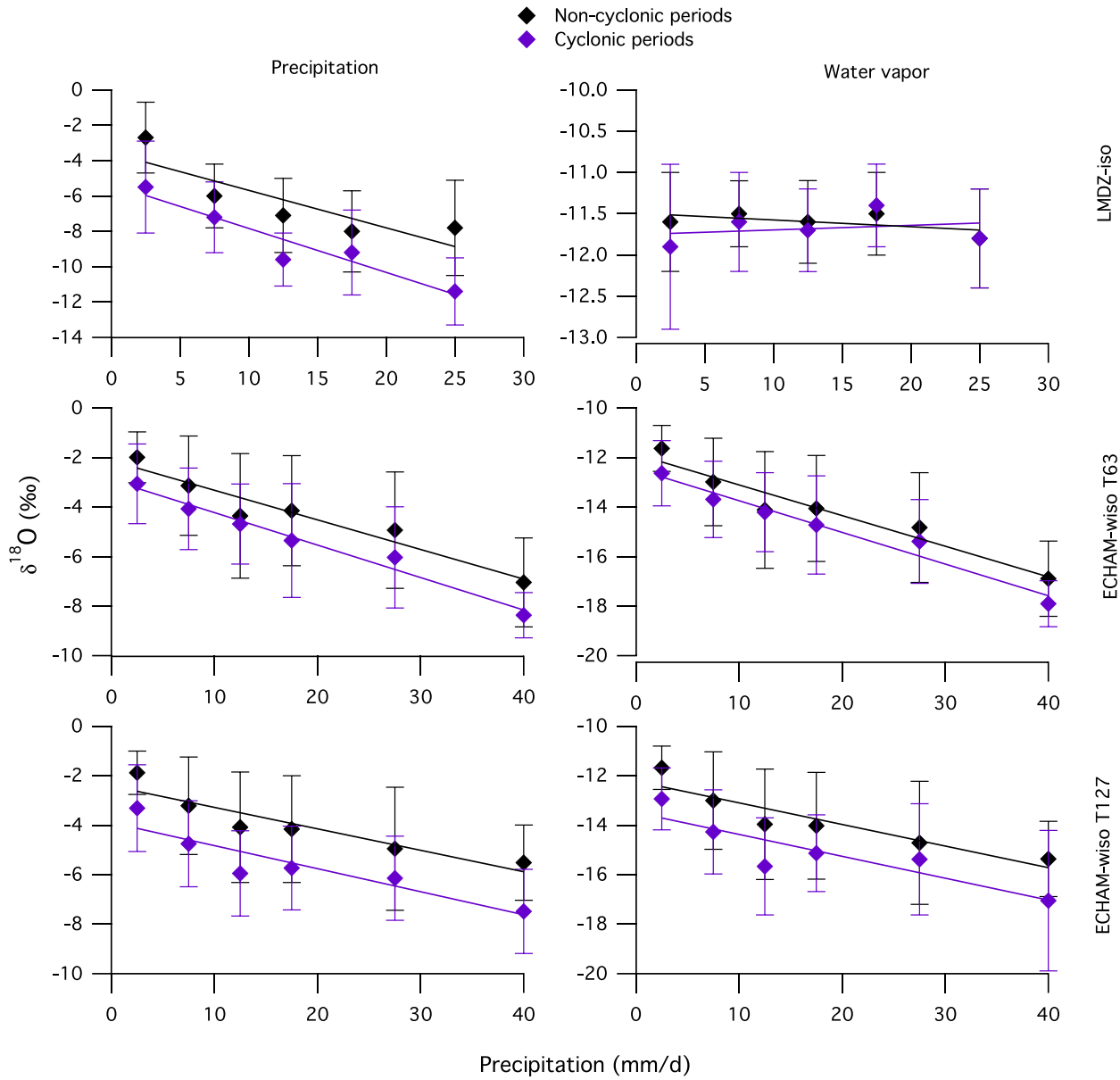

Figure 7. Isotopic composition of daily precipitation (left) and surface water vapor (right) ($\delta^{18}O_p$ and $\delta^{18}O_v$ in ‰) in LMDZ-iso and ECHAM6-iso at T63 and T127 spatial resolutions as a function of precipitation (mm/d).

Gao et al., 2013; Risi et al., 2008; Vimeux et al., 2005), this allows the depletion to accumulate more in the water vapor and subsequent precipitation.

In contrast, although LMDZ-iso also captures the amount effect and the stronger $\delta^{18}O$ depletion for cyclonic rains, the amount effect is not captured for water vapor neither at the surface level (Figure 7) nor at 790 hPa (not shown). Thus, the question arises about the processes, different from the amount effect, that are involved during the three cyclones well reproduced by LMDZ-iso. We investigate the possible role of increased large-scale precipitation during cyclones. First, for high precipitation rate (>20 mm/d), LMDZ-iso clearly simulates higher isotopic depletion in water vapor $\delta^{18}O$ (by 1‰–2‰) when the fraction of large-scale precipitation is high (>70%). Second, on average, the fraction of large-scale precipitation is higher during cyclonic periods (19%) than during non-cyclonic periods (11%) and the fraction of large-scale precipitation is higher during the three aforementioned systems (42%) than for the other low-pressure systems (11%). In LMDZ-iso, large-scale precipitation is typically more depleted than convective precipitation (Tuinenburg et al., 2015) because it is formed at a higher altitude and in moister conditions.

Previous studies showed that during tropical cyclones the enhanced diffusive exchanges between rain and water vapor and the reduced fraction of rain evaporation, both due to a more humid environment, are the main causes of the isotopic depletion in water vapor and precipitation (Lawrence et al., 2004; Risi et al., 2023). Risi et al. (2008) clearly demonstrated that interaction between both water phases controlled the amount effect (Risi et al., 2008). Our model-data comparison shows that ECHAM6-wiso well captures the amount effect and well reproduces the isotopic depletion during cyclones consistently with what we expect from previous studies. In contrast, LMDZ-iso is unable to capture the water vapor amount effect, suggesting that it underestimates the depleting effect of rain–water vapor interaction. Yet, it is able to reproduce the isotopic depletion for 3 cyclones. For LMDZ-iso, the increased fraction of large-scale precipitation during cyclones may also play a dominant role in depleting water vapor. We hypothesize that when rain–water vapor interaction is the dominant factor controlling the isotopic depletion during low-pressure systems, LMDZ-iso reproduces only partly the observations. In opposite, when the increase of large-scale precipitation dominates, LMDZ-iso model is able to reproduce the observed depletion. Further study would be needed to further investigate the causes of the differences between the two models, and the impact of the different spatial resolution and physical parametrizations.

Using the hourly resolution of observed $\delta^{18}O_v$, we explore in the next sections whether we can detect the presence of enhanced cyclone-associated processes such as enhanced diffusive exchange and low fraction of rain evaporation and if so, how they could modulate the isotopic variability within the best-track periods.

5. Discussion on Atmospheric Processes Inside Low-Pressure Systems That Isotopically Deplete Water Vapor

5.1. Description of Hourly $\delta^{18}O_v$ and d_v Variations During Cyclonic Periods

As this is the first time that hourly water vapor isotope ratios are documented for cyclones on Réunion Island, we provide in this first section a short description of the hourly data over the best-track periods. As an example, the hourly observations are shown for Carlos in Figure 8. The hourly observations for the other low-pressure systems are shown in Figure S2 in Supporting Information.

Superimposed on the V-shaped $\delta^{18}O_v$ variation, a strong hourly isotopic variability is observed during the best-track periods on timescales from a few hours to more than one day. Hourly $\delta^{18}O_v$ during best-track periods can be as high as $\delta^{18}O_v$ values in reference periods (Haliba, Carlos, Dumazile, Calvinia). The hourly lowest isotopic value during the different best-track periods varies from −22.8‰ to −40.5‰ with a mean of -28.8 ± 4.9‰ ($n = 12$).

The strong negative spikes of hourly $\delta^{18}O_v$ during low-pressure systems are often associated with positive shifts in d_v as already noted by Sun et al. (2022) ($\delta^{18}O_v$ is significantly anti-correlated with d_v during best-track periods with $r^2 = 0.35$, $n = 2171$, $p < 0.001$) (Figure S2 in Supporting Information). This is clearly illustrated during the Dumazile system where d_v increases up to ∼27‰ while $\delta^{18}O_v$ drops below −35‰ over 3 hr on 7 March 2018 and during the Fakir system where $\delta^{18}O_v$ strongly decreases by ∼20‰ over 24 hr from April 23rd to 24th, 2018 whereas d_v increases by ∼10‰ (Figures S2 in Supporting Information).

We also observe in average over precipitation intervals of 4 mm/hr from 0.2 to 28 mm/hr: (a) similar or higher values of d_v during cyclonic periods than outside (the mean d_v difference between cyclonic and non-cyclonic periods is 1.3 ± 2.1‰), with a significant increase of d_v as a function of precipitation rate of +1.6‰ per 10 mm/hr during cyclonic periods ($r^2 = 0.61$, $n = 7$ (seven 4 mm/hr-precipitation intervals between 0.2 and 28 mm/hr), $p < 0.05$, not shown) (this anti-correlation is missing outside cyclonic periods) and (b) a very significant anti-correlation between d_v and $\delta^{18}O_v$: the higher precipitation rate, the higher d_v and the lower $\delta^{18}O_v$ ($r^2 = 0.95$, $n = 7$, $p < 0.001$, not shown) (this anti-correlation is missing outside cyclonic periods).

5.2. Evolution of Hourly Data in a q_v-$\delta^{18}O_v$ Diagram

Another striking feature during cyclonic periods is the absence of the $\delta^{18}O_v$ and q_v diurnal cycles within the best-track periods (Figure 8 and Figure S2 in Supporting Information). Based on a 1-year long data set, Guilpart et al. (2017) attributed the presence of diurnal cycles outside the cyclonic periods to air masses mixing between marine water vapor lifted up the Maïdo mountain during daytime and subsiding free tropospheric air during nighttime. In a q_v-$\delta^{18}O_v$ diagram based on the 6-year long record (Figure 9), we clearly confirm that non-cyclonic and cyclonic data exhibit a different scattering.

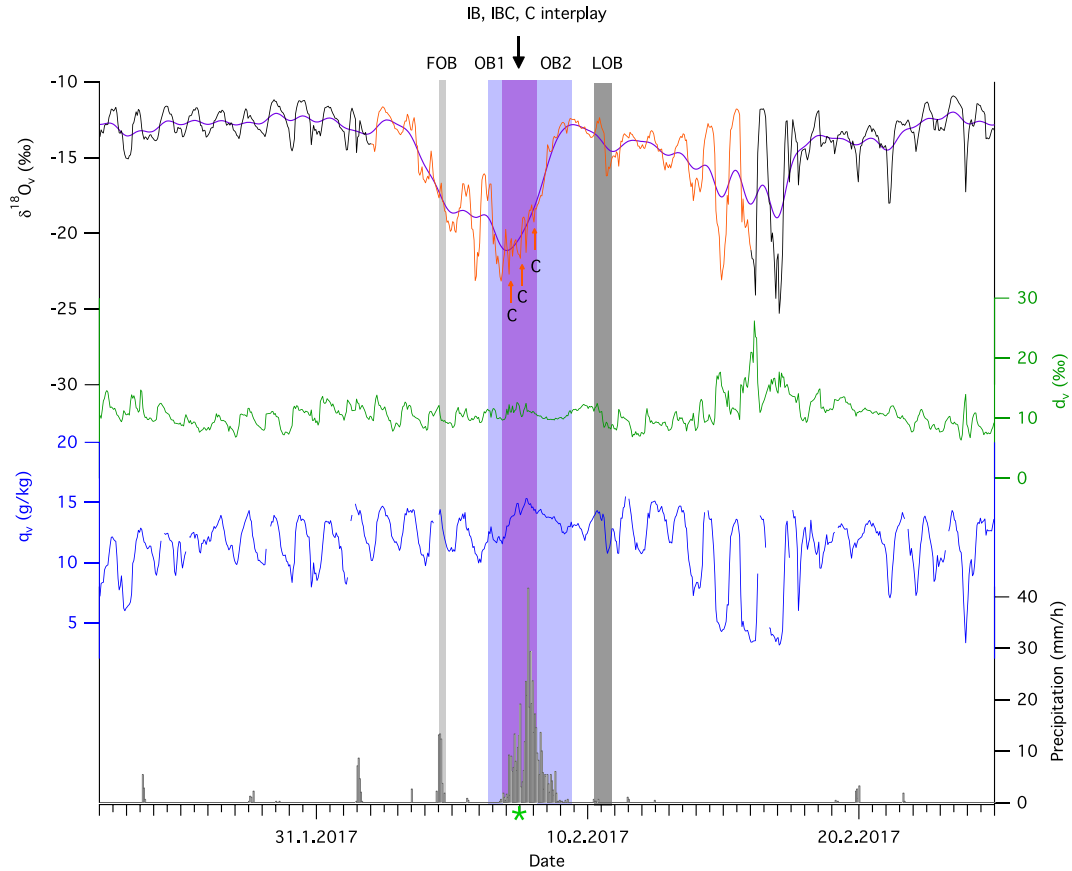

Figure 8. Hourly $\delta^{18}O_v$ (‰, the orange color indicates the best-track period), d_v (‰, green), q_v (g/kg, dark blue) and precipitation at the Maïdo station (mm/h, gray bars) for Carlos as a function of time (dd-mm-yyyy in UTC). The purple $\delta^{18}O_v$ signal is a smoothing over 5 days. The x-position of the green star indicates when the distance between the system center and the Maïdo station is minimum (here: 146 km). The different cyclonic substructures defined in Section 2.3 are represented for information: not to overload the figure, we gather inner bands (IB), convective inner bands (IBC) and convective system center (C) (the latter never lasts more than 3 hr); and OB2 is a time period where 75% of the hourly data are tagged as corresponding to a outer band (and the other 25% have no assigned substructure).

The non-cyclonic data follow a hyperbolic curve, consistent with a mixing between a marine source after lifting up the Maïdo slope of $\delta^{18}O_v = -12.8‰$ ($q \to \infty$) and a dryer and more depleted source at night. The value of $\delta^{18}O_v = -12.8‰$ is consistent with a marine vapor formed in isotopic equilibrium with the ocean and having an isotopic composition of $\delta^{18}O_v = -10.8‰$; then depleted following an altitudinal isotopic gradient of −0.1‰/100 m as it lifted up the Maïdo slope (Guilpart et al., 2017). The value of −10.8‰ is similar to the isotopic composition of marine vapor of $-10.6 \pm 0.1‰$ calculated over the reference periods according to the Merlivat and Jouzel (1979)'s equation for a smooth regime ($k_{18O} = 6‰$), using the ERA5 reanalyses (skin temperature, air temperature at 2 m, relative humidity at 2 m) averaged over an oceanic domain surrounding Réunion Island (53.875–57.125°E, 19.875–22.625°S).

In contrast, cyclonic data are preferentially isolated in the bottom right corner of the q_v-$\delta^{18}O_v$ with high values of q_v, low values of $\delta^{18}O_v$ and a sharper decrease of $\delta^{18}O_v$ with q_v. Most of the hourly data with $P_{Maïdo} > 1$ mm/hr stand below the q_v-$\delta^{18}O_v$ trajectory expected for a pure Rayleigh distillation and are consistent with super Rayleigh distillation as defined by Noone (2012) (see Figure 9 and its legend), indicating a strong remoistening by rain evaporation.

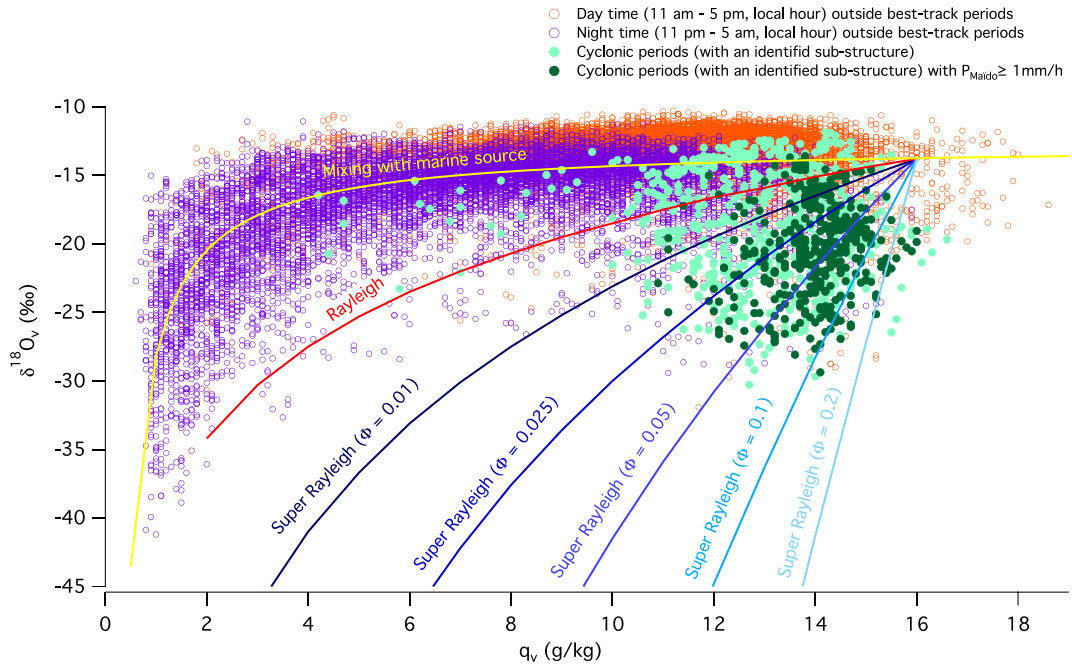

Figure 9. Hourly $\delta^{18}O_v$ (‰) of water vapor as a function of q_v (g/kg) from 1 November 2014 to 31 October 2020. Daytime (11 a.m.–5p.m., local hour) and nighttime (11 p.m.–5 a.m.) data are in orange and purple respectively. Cyclonic data are plotted when a cyclonic substructure impacts Réunion Island as defined in Section 2.3. Light (dark) green circles correspond to $P_{Maïdo} < (\geq)$ 1 mm/hr. The best hyperbolic fit for daytime and nighttime is plotted in yellow ($\delta^{18}O_v = 12.8–15.4/q$). The red curve plots data resulting from a Rayleigh distillation that assumes an original vapor of $\delta^{18}O_{v0} = -13.6‰$ and $q_0 = 16$ g/kg (calculated from the hyperbolic fit). The $\delta^{18}O_{v0}$ value is consistent with the mean $\delta^{18}O_v$ over daytime outside cyclonic periods of −13.4‰. Dark blue to light blue curves denotes a similar evolution following a super Rayleigh distillation as defined by Noone (2012) for different value of the Φ parameter (0.01–0.2) ($T = 25°C$).

5.3. Evolution of $\delta^{18}O_v$ and d_v According to the Cyclonic Substructure

Figures 10 and 11 show boxplots with composite values of hourly $\delta^{18}O_v$ and d_v for each cyclonic substructure defined in Section 2.3. While Figures 10 and 11 gather the 12 cyclones into a single composite isotopic structure, it is worth noting that it reflects the major statistical features of individual systems.

Within the storm system, we clearly observe a progressive isotopic depletion of water vapor toward the system center in agreement with previous studies (Fudeyasu et al., 2008; Gedzelman et al., 2003; Jackisch et al., 2022; Lawrence et al., 2002; Munksgaard et al., 2015; Risi et al., 2023; Sanchez-Murillo et al., 2019; Skrzypek et al., 2019; Sun et al., 2022; Xu et al., 2019). On average, the most depleted domains are the convective outer bands (OBC, $\delta^{18}O_v = -21.6 \pm 2.5‰$, $n = 322$), the convective inner band (IBC, $\delta^{18}O_v = -22.6 \pm 2.7‰$, $n = 29$), and the convective system center (C, $\delta^{18}O_v = -22.2 \pm 3.4‰$, $n = 18$). All cyclonic substructures exhibit an average $\delta^{18}O_v$ lower than the average $\delta^{18}O_v$ over the reference periods ($-15.2 \pm 3.2‰$, $n = 3{,}756$) that are considered here as representative of the environment (the spatial domain surrounding the cyclone). We also observe that water vapor in the outer and inner bands (OB and IB) is more depleted when bands are tagged as intense convective (IBC and OBC) bands by $-2.5 \pm 0.2‰$ on average. For a given substructure within the cyclone, the distribution of $\delta^{18}O_v$ is shifted toward lower values when considering only precipitating periods ($P_{Maïdo} > 1$ mm/hr): median values shown in Figure 10 are shifted on average by −2.3‰ whereas the shift for the reference periods is only −0.4‰. The more enriched $\delta^{18}O_v$ is recorded for the region in-between rain bands (IRB, $\delta^{18}O_v = -18.9 \pm 4.1‰$, $n = 172$) in agreement with previous studies showing that water vapor and rain are more depleted in rain bands than in between (Gedzelman et al., 2003; Lawrence et al., 2002; Risi et al., 2023; Sanchez-Murillo et al., 2019; Xu et al., 2019). In addition, we observe that the isotopic distribution for the bands at the edge of the system (FOB and LOB) is quite broad and includes the lowest hourly isotopic values within the cyclone. We also observe that mean values are higher for FOB and LOB ($-17.6 \pm 4.3‰$ and $-17.1 \pm 3.3‰$ respectively). Last, the FOB and LOB domains are statistically very similar as already noted by Ohsawa and Yusa (2000) who pointed out a symmetrical pattern of the isotopic composition of rain with respect to the low-pressure system center.

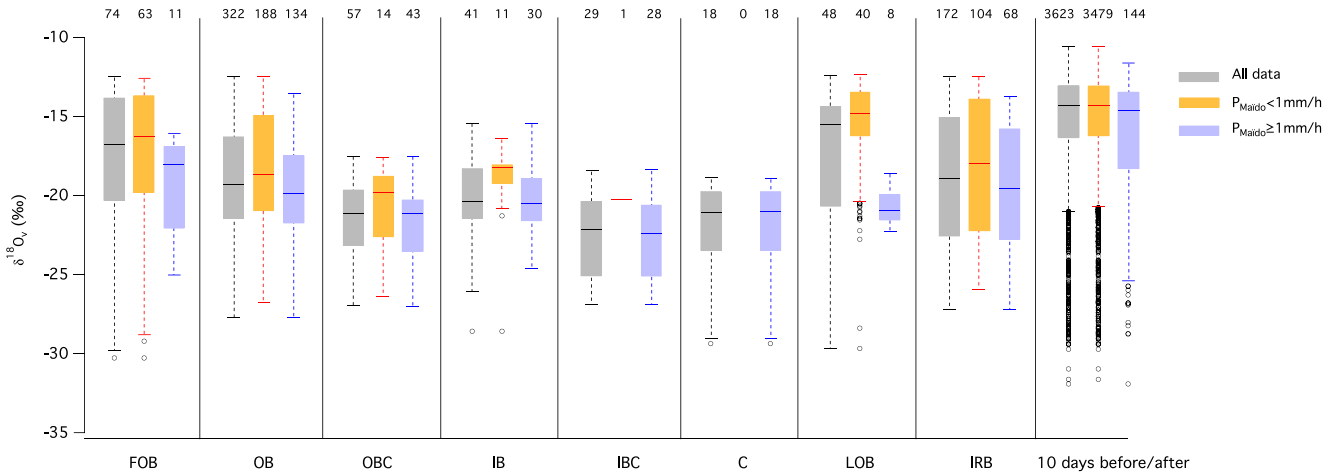

Figure 10. Boxplots for $\delta^{18}O_v$ for the different cyclonic substructures defined in Section 2.3: First outer band (FOB), Outer band (OB), Convective outer band (OBC), Inner band (IB), Convective inner band (IBC), convective zone at the system center (C), Last outer band (LOB), In-between rain bands (IRB). The statistical values are also plotted for the 10 days preceding and following the cyclonic best-track time periods (except when the latter periods overlap best-track periods of another system as for Bansi and Chedza, Ava and Berguitta, Diane and Esami). The boxplots show the median, the first (Q1) and the third (Q3) quartile, spread and outliers. The higher (lower) whisper corresponds to Q3 + 1.5•(Q3 − Q1) (Q1 − 1.5•(Q3 − Q1)) or to the maximum (minimum) value in the data set in case this maximum (minimum) value is lower (higher) than Q3 + 1.5•(Q3 − Q1) (Q1 − 1.5•(Q3 − Q1)). The number of hourly data used in the calculations is mentioned at the top of each boxplot. The number of cyclones taken into account for each substructure depends on the substructure and are: FOB (9), OB (11), OBC (5), IB (4), IBC (5), C (3), Q (5), IRB (11). The orange (purple) boxplots are done only for data with $P_{Maïdo} < (\geq)$ 1 mm/hr.

The average d_v within the reference periods (12.4 ± 2.9‰) is comparable with average d_v for the different cyclonic substructures varying from 10.4 ± 2.2‰ (IB) to 14.2 ± 3.2‰ (IBC) (Figure 11). Within the cyclonic system, the differences between the different substructures are low (Figure 11). In particular, we do not observe systematic higher deuterium excess in rain bands (OB, IB, OBC, IBC and C with mean d_v values of 12.1 ± 2.5‰, 10.4 ± 2.2‰, 12.4 ± 2.6‰, 14.2 ± 3.2‰, and 12.3 ± 4.2‰) than in between (IRB with mean d_v values of 12.7 ± 2.8‰) as observed in Munksgaard et al. (2015). However, it is worth noting that the mean d_v value in the convective IB is significantly higher than in the other bands. Interestingly, the d_v distribution shifts toward higher values during precipitating periods ($P_{Maïdo} > 1$ mm/hr) for all cyclone substructures with sufficient data, except for the IRB (in-between rain bands) which have similar d_v in precipitating and non-precipitating periods (Figure 11). Median values are shifted between 1.0 and 3.9‰ whereas the shift during the reference periods is only 0.6‰ (Figure 11).

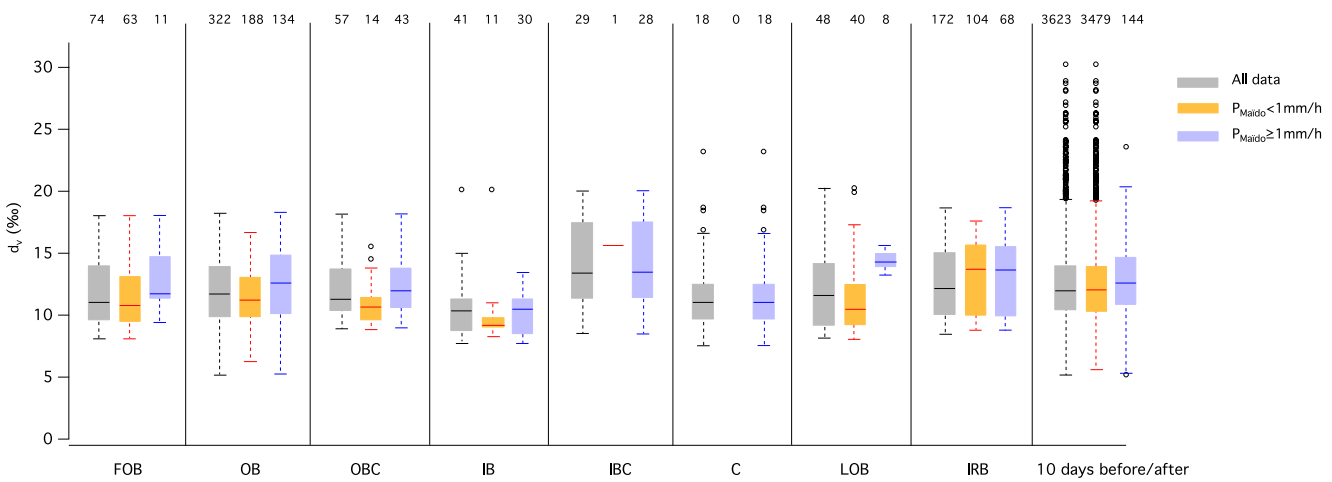

Figure 11. Same as Figure 10 but for deuterium excess in water vapor (d_v).

5.4. Description of $\delta^{18}O_p$ and d_p During and Outside Cyclonic Periods

The coarse temporal resolution of rain collected during cyclones does not allow us to describe how $\delta^{18}O_p$ and d_p vary within cyclones. However, we can compare $\delta^{18}O_p$ and d_p within and outside cyclonic periods.

During cyclonic (non-cyclonic) periods, $\delta^{18}O_p$ varied between −2.13‰ and −15.15‰ (between −12.81 and 3.55‰) (Figure 4a). The mean amount-weighted $\delta^{18}O_p$ during cyclones (outside cyclones) is -10.28 ± 1.95‰ (-5.90 ± 2.29‰).

The distribution of d_p is shifted toward low values during cyclonic periods (d_p varied from 0 to 34.8‰ outside cyclonic periods vs. −2.7 to –21.1‰ during cyclonic periods) and the mean d_p is higher during non-cyclonic periods ($d_{p\_non\text{-}cyclonic} = 17.3 \pm 5.0$‰, $n = 556$) than over cyclonic periods ($d_{p\_cyclonic} = 13.2 \pm 3.5$‰, $n = 61$). In addition, for a given interval of precipitation, d_p is always lower for cyclonic rains and it decreases with increasing precipitation (as already noted by Sun et al., 2022): for $0.1 < P < 10$ mm, $d_{p\_non\text{-}cyclonic} = 17.9 \pm 5.0$‰ and $d_{p\_cyclonic} = 13.9 \pm 4.8$‰; for $10 \leq P < 50$ mm, $d_{p\_non\text{-}cyclonic} = 14.4 \pm 2.9$‰ and $d_{p\_cyclonic} = 13.4 \pm 2.1$‰; for $P \geq 50$ mm, $d_{p\_non\text{-}cyclonic} = 13.3 \pm 4.2$‰ and $d_{p\_cyclonic} = 12.1 \pm 1.9$‰; and for $P \geq 200$ mm, $d_{p\_cyclonic} = 11.3 \pm 2.9$‰ (one non-cyclonic rain at $d_{p\_non\text{-}cyclonic} = 8.8$‰) (see also Figure S3a in Supporting Information).

At last, a significant positive relationship between $\delta^{18}O_p$ and d_p for cyclonic precipitation ($r^2 = 0.25$, $n = 61$) is found whereas this correlation is not observed over non-cyclonic rains ($r^2 < 0.001$, $n = 617$) (Figure S3b in Supporting Information).

5.5. Consequences for Atmospheric Processes at Play

5.5.1. Rain Evaporation and Diffusive Rain–Vapor Exchanges

Previous observational and simple box modeling studies have highlighted the dominant role of rain evaporation and rain–water vapor diffusive exchanges in depleting water vapor within convective organized systems (Lawrence et al., 2004; Risi et al., 2021, 2023; Tremoy et al., 2014; Xu et al., 2019). Rain evaporation acts to deplete the water vapor when the fraction of the evaporated raindrop is low. Indeed, light isotopes preferentially evaporate and consequently the rain evaporation flux toward surrounding water vapor is depleted, and in most cases more depleted than the surrounding vapor as rain usually forms a higher altitude than that at which it evaporates. The evaporation flux is more depleted as the fraction of evaporated rain is smaller (Stewart, 1975; Tremoy et al., 2014). In the limit case where rain drops totally evaporate, the evaporation flux has the same isotopic composition as the rain drop. Since rain drops are typically more enriched than the vapor, total evaporation of rain drops has an enriching effect on the vapor. In moist conditions as is the case here, the fraction of rain drops that evaporate is small, and thus rain evaporation has a depleting effect. This depleting effect is strongest when the evaporation flux (not fraction) is large. This is why for a given evaporated fraction, large rainfall rates are expected to be associated with a larger depletion by rain evaporation (Worden et al., 2007). Last, moist environment favors rain–water vapor diffusive exchanges. As rain usually forms at a higher altitude than that at which water vapor-rain exchanges take place, its isotopic composition is usually lower than that in equilibrium with low-level water vapor into which it falls. As a consequence, enhanced rain–water diffusive exchanges favor the isotopic depletion of water vapor.

Our study provides a body of evidence that evaporation with small fraction of evaporate and rain–vapor diffusive exchanges are present within the low-pressure systems and could explain the higher isotopic depletion of both water vapor and rain inside tropical cyclones:

1. We observe much depleted water vapor in the most convective bands within all studied low-pressure systems. This depletion under humid conditions is likely induced by the presence of a stratiform area with low proportion of rain evaporation of very depleted rain formed at high level and resulting from snow melting as already suggested by Risi et al. (2021).
2. Most of the hourly data (96%) associated with a rainy cyclonic substructure are explained by super Rayleigh trajectories in a q_v-$\delta^{18}O_v$ diagram (Figure 9) showing that rain evaporation is at play to explain the isotopic composition of water vapor. The fraction of evaporated rain (f) can be estimated from the Φ values used in Figure 9 to plot the super Rayleigh curves encompassing the observations. In the line of Noone (2012), we describe in the supplementary information how the Φ parameter evolves as a function of the fraction of evaporated rain. However, instead of using Craig and Gordon (1965) to describe the isotopic composition of the

evaporated flux as evaporation proceeds, we use here the equation from Stewart (1975) (see Supplementary Information Text S1). This enables us to account for the fact that the isotopic composition of the evaporated flux depends on the fraction of evaporated rain. The estimated evaporated fraction varies from 2% ($\Phi \sim 0.01$) to more than 75% ($\Phi > 0.2$) with 60% (80%) of hourly data corresponding to $f < 15\%$ (32%) and only 2% corresponding to $f > 75\%$ ($T = 20°C$, $h = 0.7$, see Supplementary Information Text S1).

3. The observation that lowest values of $\delta^{18}O_v$ were accompanied by positive shifts in d_v, the higher values of d_v in raining cyclonic substructures and the correlated decreasing of $\delta^{18}O_v$ with increasing d_v as precipitation rate increases are consistent with the expected effect of rain evaporation (since $HD^{16}O$ diffuses faster than $H_2{}^{18}O$) in humid conditions and with low fraction of rain evaporation. This is well illustrated by the curves showing the combined evolution of $\delta^{18}O_v$ and d_v as a function of the increasing fraction of evaporated rain according to the Stewart's theory (Stewart, 1975; see also Figure 4 in Tremoy et al., 2014; and Figure 5 in Penchenat et al., 2020).
4. The shift of d_p values toward lower values during best-track periods and the general decrease of d_p as precipitation rate increases and as $\delta^{18}O_p$ decreases may reflect a low fraction of evaporation in downdrafts during deep convection as already suggested by Risi et al. (2008, 2020).
5. According to Risi et al. (2023), rain evaporation favors the isotopic depletion of water vapor which accumulates as air moves inward. We actually observe that IB and IBC bands are more depleted than OB and OBC bands.
6. In the same line, the fact that water vapor is more depleted in rain bands than in between may reflects evaporation of highly depleted rain originating from higher altitude (Risi et al., 2021).

5.5.2. Condensation and Convection Intensity

Because water vapor is depleted even in the non-precipitating parts of rain bands and convective regions relative to the environment (Figure 10, orange bars) local condensation and precipitation is likely not the dominant control on the pronounced isotopic depletion from the edge to the system center as also shown by Risi et al. (2023). However, the convective deepness and the likely presence of a stratiform zone may have an influence as rain bands tagged as convective (IBC and OBC) are more depleted than the non-convective rain bands (IB and OB respectively) (the difference of tagging being on the brightness temperature and thus on the depth of convection). This is consistent with Risi et al. (2021) who suggested that low evaporation of droplets depletes water vapor more efficiently when the droplets originate from snow formed at high levels. The higher altitude of condensation during cyclones could thus partly explain a stronger depletion during deep convection.

5.5.3. Summary

We have evidenced that within the studied low-pressure systems, rain evaporation tends to deplete $\delta^{18}O_v$ and to increase d_v. This process is especially present in the stratiform part of mesoscale convective systems and can thus contribute to the isotopic depletion during cyclones. Risi et al. (2021) proposed to conciliate both large-scale and local processes: storm activity associated with regimes of large-scale ascent is associated with moister conditions. The enhanced precipitation induces a progressive isotopic depletion of water vapor by increasing water vapor-rain interaction. When relative humidity is larger, less snow sublimates before melting leading to very depleted precipitation at lower levels, a smaller fraction of rain evaporates, and diffusive exchanges are favored. These processes eventually lead to more depleted water vapor.

6. Conclusion

Our documentation of $\delta^{18}O_p$ over 6 years from 2014 to 2020 in Réunion Island shows that the annual $\delta^{18}O_p$ is strongly controlled by the number of cyclones, the number of best-track days, and the proportion of cyclonic rain during the year. Our study thus supports the use of $\delta^{18}O_p$ in annual-resolved tropical climate archive as a proxy of past cyclone frequency (Baldini et al., 2016; Medina-Elizalde & Rohling, 2012; Nott et al., 2007). Our observations also show that the isotopic depletion during cyclonic periods is stronger, thus agreeing with previous observations of more depleted precipitation and water vapor in the vicinity of tropical cyclones relative to less organized convective systems.

Among the two isotope-enabled AGCMs studied here, the pronounced depletion in daily-averaged $\delta^{18}O_v$ recorded during the passage of low-pressure systems and the stronger isotopic depletion during low-pressure systems, are mainly captured by ECHAM6-wiso, clearly demonstrating the key role of large-scale atmospheric processes in

depleting efficiently the isotopic composition of water vapor. Risi et al. (2023) concluded that the main factor depleting the water vapor isotopic ratio in mesoscale convective systems is rain evaporation, and that enhanced water vapor-precipitation interactions in a humid environment in the vicinity of tropical cyclones explain the more depleted rain observed in tropical cyclones relative to small-scale convection. Our observations do not contradict this conclusion. Actually, ECHAM6-wiso well captures on average the interaction between water vapor and precipitation since it captures the amount effect, which is mainly controlled by these interactions (Risi et al., 2008). The mesoscale circulation reshapes the spatial patterns of isotope anomalies within the cyclones, but is not necessary to capture the mean anomaly associated with a cyclone at the daily scale. The lack of the amount effect on $\delta^{18}O_v$ in LMDZ-iso can explain that this model does not reproduce the V-shaped $\delta^{18}O_v$ for 9 of the 12 low-pressure systems. Nonetheless, the correct reproduction of the isotopic depletion for three systems illustrates that other processes can be involved in the higher isotopic depletion within tropical cyclones. Indeed, we found that, on average, the proportion of large-scale precipitation is larger during cyclones in LMDZ-iso and that large-scale precipitation is characterized by lower isotopic ratios in the model.

Our observations suggest that rain evaporation and diffusive exchanges between rain and water vapor could be responsible also of the short-term isotopic variability superimposed on the synoptic V-shaped $\delta^{18}O_v$, in relation with the sampled cyclonic substructure. This points out the potential of water isotopes ratio to bring fundamental information on atmospheric processes such as the proportion of evaporated rain within downdrafts although major constraints remain to this at present. To better quantify the relative importance of processes at play in determining the isotopic composition of water vapor in the different subdomains inside cyclones, a conceptual model of water and isotopic budget or a realistic cyclonic simulation using a cloud-resolving model enabled with water stable isotopes would be useful. In addition, it is clear that to investigate the impact of rain–vapor interactions on the isotopic composition of both the vapor and rain, ideally we should compare the isotopic composition of the water vapor to that in equilibrium with the rain (Graf et al., 2019; Vimeux & Risi, 2021). However, cyclonic rains were sampled over extended periods, including periods of several hours without any rain. This complicates the comparison between the rain and the water vapor composition over these periods. This study points out the need of higher temporal resolution for collected precipitation that would allow us to deepen the discussion.

Data Availability Statement

The isotopic composition of precipitation and water vapor as well as the LMDZ-iso and ECHAM6-wiso simulations used in this study are available on the Zenodo repository at Vimeux (2023). The Météo-France/DIROI RSMC best-tracks and BCMOM are available on Météo-France website at Météo-France/DIROI (2023a, 2023b). The GPM precipitation products are available on GES DISC website at Iguchi and Meneghini (2021). The NCEP/CPC 4-km pixel resolution IR brightness temperature are available on GES DISC website at Janowiak et al. (2017). The ERA5 dataset used in this study is available on the Copernicus Climate data store at Hersbach et al. (2023).

Acknowledgments
We deeply thank Jean-Luçay Felix, Eric Golubic, Patrick Hernandez, and Louis Mottet for collect of precipitation at the Maïdo atmospheric observatory between 2014 and 2020. The precipitation data at the Piton Maïdo station were provided by AERIS/ESPRI (Ensemble des Services Pour la Recherche à l'IPSL/Pôle de données et services pour l'atmosphère) from 2018 and by the Météo-France-DIROI (Direction Inter-Régionale de Météo-France pour l'Océan Indien) before 2018. The best-track periods dataset was provided by the RSMC La Réunion. We also deeply thank François Bonnardot at Météo-France-DIROI for fruitful discussions. The LMDZ-iso simulation was performed using HPC ressources from GENCI-IDRIS (project 7632). This study was funded by the ANR proposal ISOTROPIC 12-BS06-001, by the CNRS-INSU LEFE (Les Enveloppes Fluides et l'Environnement) program and by the Institut de Recherche pour le Développement (IRD). The instrument benefits from the OPAR (Observatoire de Physique de l'Atmosphère à La Réunion) infrastructure funded by CNRS-INSU and Université de La Réunion and managed by OSU-R (Observatoire des Sciences de l'Univers à La Réunion, UAR 3365). We thank S.K. Bhattacharya and two anonymous reviewers for their very fruitful comments that improved the manuscript.

References

Aggarwal, P. K., Romatschke, U., Araguas-Araguas, L., Belachew, D., Longstaffe, F. J., Berg, et al. (2016). Proportions of convective and stratiform precipitation revealed in water isotope ratios. *Nature Geosciences*, *9*, 624–629. https://doi.org/10.1038/ngeo2739

Ansari, A., Noble, J., Deodhar, A., Mendhekar, G. N., & Jahan, D. (2020). Stable isotopic ($\delta^{18}O$ and $\delta^{2}H$) and geospatial approach for evaluating extreme rainfall events. *Global and Planetary Change*, *194*. 103299. https://doi.org/10.1016/j.gloplacha.2020.103299

Astier, N., Plu, M., & Claud, C. (2015). Associations between tropical cyclone activity in the Southwest Indian Ocean and El Nino Southern Oscillation. *Atmospheric Science Letters*, *16*(4), 506–511. https://doi.org/10.1002/asl.589

Baldini, L. M., Baldini, J. U., McElwaine, J. N., Frappier, A. B., Asmerom, Y., Liu, K.-B., et al. (2016). Persistent northward North Atlantic tropical cyclone track migration over the past five centuries. *Scientific Reports*, *6*(1), 37522. https://doi.org/10.1038/srep37522

Baray, J. L., Courcoux, Y., Kechut, P., Portafaix, T., Tulet, P., Cammas, J. P., et al. (2013). Maïdo observatory: A new high-altitude station facility at Reunion Island (21°S, 55°E) for long-term atmospheric remote sensing and in situ measurements. *Atmospheric Measurement Techniques*, *6*(10), 2865–2877. https://doi.org/10.5194/amt-6-2865

Bessafi, M., & Wheeler, M. C. (2006). Modulation of south Indian Ocean tropical cyclones by the Madden-Julian oscillation and convectively-coupled equatorial waves. *Monthly Weather Review*, *134*(2), 638–656. https://doi.org/10.1175/MWR3087.1

Bhattacharya, S. K., Sarkar, A., & Liang, M.-C. (2022). Vapor isotope probing of typhoons invading the Taiwan region in 2016. *Journal of Geophysical Research: Atmospheres*, *127*(21). https://doi.org/10.1029/2022JD036578

Bieli, M., Camargo, S. J., Sobel, A. H., Evans, J. L., & Hall, T. (2019). A global climatology of extratropical transition. Part I: Characteristics across basins. *Journal of Climate*, *32*(12), 3557–3582. https://doi.org/10.1175/JCLI-D-17-0518.1

Bloemendaal, N., de Moel, H., Martinez, A. B., Muis, S., Haigh, I. D., van der Wiel, K., et al. (2022). A globally consistent local-scale assessment of future tropical cyclone risk. *Science Advances*, *8*(17). https://doi.org/10.1126/sciadv.abm8438

Cauquoin, A., & Werner, M. (2021). High-resolution nudged isotope modeling with ECHAM6-wiso: Impacts of updated model physics and ERA5 reanalysis data. *Journal of Advances in Modeling Earth Systems*, *13*(11), e2021MS002532. https://doi.org/10.1029/2021MS002532

Cauquoin, A., Werner, M., & Lohmann, G. (2019). Water isotopes-Climate relationships for the mid-Holocene and preindustrial period simulated with an isotope-enabled version of MPI-ESM. *Climate of the Past*, *15*(6), 1913–1937. https://doi.org/10.5194/cp-15-1913-2019

Chan, K. T. F., & Chan, J. C. L. (2012). Size and strength of tropical cyclones as inferred from QuickSCAT data. *Monthly Weather Review*, *140*(3), 811–824. https://doi.org/10.1175/MWR-D-10-05062.1

Chang-Seng, D. S., & Jury, M. R. (2010). Tropical cyclones in the SW Indian ocean. Part 1: Inter-annual variability and statistical prediction. *Meteorology and Atmospheric Physics*, *106*(3–4), 149–162. https://doi.org/10.1007/s00703-009-0055-2

Chen, F., Huang, C., Lao, Q., Zhang, S., Chen, C., Zhou, X., et al. (2021). Typhoon control of precipitation dual isotopes in southernChina and its palaeoenvironmental implications. *Journal of Geophysical Research: Atmospheres*, *126*(14), e2020JD034336. https://doi.org/10.1029/2020JD034336

Coindreau, O., Hourdin, F., Haeffelin, M., Mathieu, A., & Rio, C. (2007). Assessment of physical parameterizations using a global climate model with stretchable grid and nudging. *Monthly Weather Review*, *135*(4), 1474–1489. https://doi.org/10.1175/MWR3338.1

Craig, H., & Gordon, L. I. (1965). Deuterium and oxygen-18 variations in the ocean and the marine atmosphere. Spoleto, Italy. In E. Tongiorgi (Ed.), *Proceedings of a conference on stable isotopes in oceanographic studies and paleotemperatures* (pp. 9–130).

Dansgaard, W. (1964). Stable isotopes in precipitation. *Tellus*, *16*(4), 436–468. https://doi.org/10.3402/tellusa.v16i4.8993

Drake, L. (2012). Scientific prerequisites to comprehension of the tropical cyclones forecast: Intensity, track and size. *Weather and Forecasting*, *27*(2), 462–472. https://doi.org/10.1175/WAF-D-11-00041.1

Field, R. D., Jones, D. B. A., & Brown, D. P. (2010). The effects of post-condensation exchange on the isotopic composition of water in the atmosphere. *Journal of Geophysical Research*, *115*(D24), D24305. https://doi.org/10.1029/2010JD014334

Frappier, A. B., Sahagian, D., Carpenter, S. J., González, L. A., & Frappier, B. R. (2007). Stalagmite stable isotope record of recent tropical cyclone events. *Geology*, *35*(2), 111–114. https://doi.org/10.1130/G23145A.1

Fudeyasu, H., Ichiyanagi, K., Sugimoto, A., Yoshimura, K., Ueta, A., Yamanaka, M. D., & Ozawa, K. (2008). Isotope ratios of precipitation and water vapor observed in Typhoon Shanshan. *Journal of Geophysical Research*, *113*(D12), D12113. https://doi.org/10.1029/2007JD009313

Gao, J., Masson-Delmotte, V., Risi, C., He, Y., & Yao, T. (2013). What controls precipitation δ18O in the southern Tibetan plateau at seasonal and intra-seasonal scales? A case study at Lhasa and Nyalam. *Tellus B: Chemical and Physical Meteorology*, *65*(1), 21043. https://doi.org/10.3402/tellusb.v65i0.21043

Gates, W. L., Boyle, J. S., Covey, C., Dease, C. G., Doutriaux, C. M., Drach, R. S., et al. (1999). An overview of the results of the Atmopsheric Model Intercomparison Project (AMIP I). *Bulletin of the American Meteorological Society*, *80*(1), 29–55. https://doi.org/10.1175/1520-0477(1999)080<0029:AOOTRO>2.0CO;2

Gedzelman, S., Lawrence, J., Gamache, J., Black, M., Hindman, E., Black, R., et al. (2003). Probing hurricanes with stable isotopes of rain and water vapor. *Monthly Weather Review*, *131*(6), 112–1127. https://doi.org/10.1175/1520-0493

Graf, P., Wernli, H., Pfahl, S., & Sodemann, H. (2019). A new interpretative framework for below-cloud effects on stable isotopes in vapour and rain. *Atmospheric Chemistry and Physics*, *19*(2), 747–765. https://doi.org/10.5194/acp-19-747-2019

Guilpart, E., Vimeux, F., Evan, S., Brioude, J., Metzger, J.-M., Barthe, C., et al. (2017). The isotopic composition of near-surface water vapor at the Maïdo observatory (Reunion Island, southwestern Indian Ocean) documents the controls of the humidity of the subtropical troposphere. *Journal of Geophysical Research: Atmospheres*, *122*(18), 9628–9650. https://doi.org/10.1002/2017JD026791

Hersbach, H., Bell, B., Berrisford, P., Biavati, G., Horányi, A., Muñoz Sabater, J., et al. (2023). ERA5 hourly data on single levels from 1940 to present. [Dataset] Copernicus Climate Change Service (C3S) Climate Data Store (CDS). https://doi.org/10.24381/cds.adbb2d47

Hersbach, H., Bell, B., Berrisford, P., Hirahara, S., Horanyi, A., Muñoz-Sabater, J., et al. (2020). The ERA5 global reanalysis. *Quarterly Journal of the Royal Meteorological Society*, *146*(730), 1999–2049. https://doi.org/10.1002/qj.3803

Holland, G. J. (1993). *Ready reckoner, chapter 9, global guide to tropical cyclone forecasting*. WMO/TC-n°560, reports n° TCP-31. World Meteorological Organization.

Hourdin, F., Rio, C., Grandpeix, J. Y., Madeleine, J. B., Cheruy, F., Rochetin, N., Ghattas, J., et al., (2020). LMDZ6A: The atmospheric component of the IPSL climate model with improved and better tuned physics. *Journal of Advances in Modeling Earth Systems*, *12*(7), e2019MS001892. https://doi.org/10.1029/2019MS001892

Houze, R. A. (2010). Clouds in tropical cyclones. *Monthly Weather Review*, *138*(2), 293–344. https://doi.org/10.11175/2009MWR2989.1

Iguchi, T., & Meneghini, R. (2021). GPM DPR precipitation profile L2A 1.5 hours 5 km V07. [Dataset], Greenbelt, MD, Goddard Earth Sciences Data and Information Services Center (GES DISC). https://doi.org/10.5067/GPM/DPR/GPM/2A/07

IPCC. (2021). In V. Masson-Delmotte, P. Zhai, A. Pirani, S. L. Connors, C. Péan, et al. (Eds.), *Climate change 2021: The physical science basis. Contribution of working group I to the sixth assessment report of the intergovernmental panel on climate change*. Cambridge University Press. https://doi.org/10.1017/9781009157896

Jackisch, D., Yeo, B. X., Switzer, A. D., He, S., Cantarero, D. L. M., Siringan, F. P., & Goodkin, N. F. (2022). Precipitation stable isotopic signatures of tropical cyclones in metropolitan manila, Philippines, show significant negative isotopic excursions. *Natural Hazards and Earth System Sciences*, *22*(1), 213–226. https://doi.org/10.5194/nhess-22-213-2022

Janowiak, J. E., Joyce, R. J., & Xie, P. (2017). NCEP/CPC L3 half hourly 4km global (60S–60N) merged IR V1. [Dataset]. In A. Savtchenko, & M. D. Greenbelt (Eds.). Goddard earth Sciences data and information services center (GES DISC). https://doi.org/10.5067/P4HZB9N27EKU

Kimball, S. K., & Mulekar, M. S. (2004). A 15-year climatology of North Atlantic tropical cyclones. Part I: Size parameters. *Journal of Climate*, *17*(18), 3555–3575. https://doi.org/10.1175/1520-0442(2004)017<3555:AYCONA>2.0.CO;2

Knapp, K. R., Kruk, M. C., Levinson, D. H., Diamond, H. J., & Neumann, C. J. (2010). The international best track archive for climate stewardship (IBTrACS). *Bulletin of the American Meteorological Society*, *91*(3), 363–376. https://doi.org/10.1175/2009BAMS2755.1

Knutson, T., Camargo, S. J., Chan, J. C., Emanuel, K., Ho, C.-H., Kossin, J., et al. (2020). Tropical cyclones and climate change assessment: Part II: Projected response to anthropogenic warming. *Bulletin of the American Meteorological Society*, *101*(3), E303–E322. https://doi.org/10.1175/BAMS-D-18-0194.1

Kuleshov, Y., Ming, F. C., Qi, L., Chouaibou, I., Hoareau, C., & Roux, F. (2009). Tropical cyclone genesis in the Southern Hemisphere and its relationship with the ENSO. *Annales Geophysicae*, *27*(6), 2523–2538. https://doi.org/10.5194/angeo-27-2523-2009

Kuleshov, Y., Qi, L., Fawcett, R., & Jones, D. (2008). On tropical cyclone activity in the Southern Hemisphere: Trends and the ENSO connection. *Geophysical Research Letters*, *35*(14). https://doi.org/10.1029/2007GL032983

Kurita, N. (2013). Water isotopic variability in response to mesoscale convective system over the tropical ocean. *Journal of Geophysical Research : Atmosphere*, *118*(18), 10376–10390. https://doi.org/10.1002/jgrd.50754

Lacour, J. L., Risi, C., Worden, J., Clerbaux, C., & Coheur, P. F. (2018). Importance of depth and intensity of convection on the isotopic composition of water vapor as seen from IASI and TES δD observations. *Earth and Planetary Science Letters*, *481*, 387–394. https://doi.org/10.5194/acp-17-9645-2017

Lawrence, J. R., Gedzelman, S. D., Dexheimer, D., Cho, H.-K., Carrie, G. D., Gasparini, R., et al. (2004). Stable isotopic composition of water vapor in the tropics. *Journal of Geophysical Research*, *109*(D6), D06115. https://doi.org/10.1029/2003JD004046

Lawrence, J. R., Gedzelman, S. D., Gamache, J., & Black, M. (2002). Stable isotope ratios: Hurricane Olivia. *Journal of Atmospheric Chemistry*, *41*(1), 67–82. https://doi.org/10.1023/A:1013808530364

Lee, J.-E., & Fung, I. (2008). "Amount effect" of water isotopes and quantitative analysis of post-condensation processes. *Hydrological Processes*, *22*, 1–8. https://doi.org/10.1002/hyp.6637

LeGrande, A. N., & Schmidt, G. A. (2006). Global gridded data set of the oxygen isotopic composition in seawater. *Geophysical Research Letters*, *33*(12), L12604. https://doi.org/10.1029/2006gl026011

Leroux, M.-D., Meister, J., Mekies, D., Dorla, A.-L., & Caroff, P. (2018). A Climatology of Southwest Indian Ocean Tropical Systems: Their number, tracks, impacts, sizes, empirical maximum potentiel intensity, ad intensity changes. *Journal of Applied Meteorology and Climatology*, *57*(4), 1021–1041. https://doi.org/10.1175/JAMC-D-17-0094.1

Li, Z. W., & O'Gorman, P. A. (2020). Response of vertical velocities in extratropical precipitation extremes to climate change. *Journal of Climate*, *33*(16), 7125–7139. https://doi.org/10.1175/JCLI-D-19-0766.1

Medina-Elizalde, M., & Rohling, E. J. (2012). Collapse of Classic Maya civilization related to modest reduction in precipitation. *Science*, *335*(6071), 956–959. https://doi.org/10.1126/science.1216629

Merlivat, L., & Jouzel, J. (1979). Global climatic interpretation of the Deuterium-Oxygen 18 relationship for precipitation. *Journal of Geophysical Research*, *84*(C8), 5029–5332. https://doi.org/10.1029/JC084iC08p05029

Merrill, R. T. (1984). A comparison of large and small tropical cyclones. *Monthly Weather Review*, *112*(7), 1408–1418. https://doi.org/10.1175/1520-0493(1984)112<1408:ACOLAS>2.0.CO;2

Météo-France/DIROI (2023a). Regional Specialized meteorological centre (RSMC) best-track. [Dataset]. http://www.meteo.fr/temps/domtom/La_Reunion/webcmrs9.0/anglais/index.html

Météo-France/DIROI (2023b). Bulletins climatiques mensuels des outres-mers (BCMOM). [Dataset]. https://donneespubliques.meteofrance.fr/?fond=produit&id_produit=129&id_rubrique=52

Munksgaard, N. C., Zwart, C., Kurita, N., Bass, A., Nott, J., & Bird, M. I. (2015). Stable isotope anatomy of tropical cyclone Ita, north-eastern Australia, April 2014. *PLoS One*, *10*(3), e0119728. https://doi.org/10.1073/pnas.1719967115

Noone, D. (2012). Pairing measurements of the water vapor isotope ratio with humidity to deduce atmospheric moistening and dehydratation in the tropical midtropophere. *Journal of Climate*, *25*(13), 4476–4494. https://doi.org/10.1175/JCLI-D-11-00582.1

Nott, J., Haig, J., Neil, H., & Gillieson, D. (2007). Greater frequency variability of landfalling tropical cyclones at centennial compared to seasonal and decadal scales. *Earth and Planetary Science Letters*, *255*(3–4), 367–372. https://doi.org/10.1016/j.epsl.2006.12.023

Ohsawa, S., & Yusa, Y. (2000). Isotopic characteristics of typhonic rainwater: Typhoons N°13 (1993) and n°6 (1996). *Limnology*, *1*(2), 143–149. https://doi.org/10.1007/s102010070021

Penchenat, T., Vimeux, F., Daux, V., Cattani, O., Viale, M., Villalba, R., et al. (2020). Isotopic equilibrium between precipitation and water vapor in Northern Patagonia and its consequences on δ^{18}Ocellulose estimate. *Journal of Geophysical Research: Biogeosciences*, *125*(3). https://doi.org/10.1029/2019JG005418

Quetelard, H., Bessemoulin, P., Cerveny, R. S., Peterson, T. C., Burton, A., & Boodhooo, Y. (2009). World-record rainfalls during tropical cyclone Gamede. *Bulletin of the American Meteorology Society*, *90*(5), 603–607. https://doi.org/10.1175/20008BAMS2660.1

Risi, C., Bony, S., & Vimeux, F. (2008). Influence of convective processes on the isotopic composition of precipitation and water vapor in the tropics: 2. Physical interpretation of the amount effect. *Journal of Geophysical Research: Atmospheres*, *113*(D19). https://doi.org/10.1029/2008JD009943

Risi, C., Bony, S., Vimeux, F., & Jouzel, J. (2010). Water-stable isotopes in the LMDZ4 general circulation model: Model evaluation for present-day and past climates and applications to climatic interpretations of tropical isotopic records. *Journal of Geophysical Research: Atmospheres*, *115*(D12), D12118. https://doi.org/10.1029/2009JD013255

Risi, C., Muller, C., & Blossey, P. (2020). What controls the water vapor isotopic composition near the surface of tropical oceans? Results from an analytical model constrained by large-eddy simulations. *Journal of Advances in Modeling Earth Systems*, *12*(8). https://doi.org/10.1029/2020MS002106

Risi, C., Muller, C., & Blossey, P. (2021). Rain evaporation, snow melt, and entrainment at the heart of water vapor isotopic variations in the tropical troposphere, according to large-eddy simulations and a two-column model. *Journal of Advances in Modeling Earth Systems*, *13*(4). https://doi.org/10.1029/2020MS002381

Risi, C., Muller, C., Vimeux, F., Blossey, P., Védeau, G., Dufaux, C., & Abramian, S. (2023). What controls the mesoscale variations in water isotopic composition within tropical cyclones and squall lines? Cloud resolving model simulations in radiative-convective equilibrium. *Journal of Advances in Modeling Earth Systems*, *15*(4). https://doi.org/10.1029/2022MS003331

Sanchez-Murillo, R., Duran-Quesada, A., Esquivel-Hernandez, G., Rojas-Cantillano, D., Birkel, C., Welsh, K., et al. (2019). Deciphering key processes controlling rainfall isotopic variability during extreme tropical cyclones. *Nature Communications*, *10*(1), 4321. https://doi.org/10.1038/s41467-019-12062-3

Seneviratne, S. I., Zhang, X., Adnan, M., Badi, W., Dereczynski, C., Di Luca, A., et al. (2021). Weather and climate extreme events in a changing climate. In V. Masson-Delmotte, P. Zhai, A. Pirani, S. L. Connors, C. Péan, S. Berger, et al. (Eds.), *Climate change 2021: The physical science basis. Contribution of working group I to the sixth assessment report of the intergovernmental panel on climate change* (pp. 1513–1766). Cambridge University Press. https://doi.org/10.1017/9781009157896.013

Skrzypek, G., Dogramaci, S., Page, G. F., Rouillard, A., & Grierson, P. F. (2019). Unique stable isotope signatures of large cyclonic events as a tracer of soil moisture dynamics in the semiarid subtropics. *Journal of Hydrology*, *578*, 124124. https://doi.org/10.1016/j.jhydrol.2019.124124

Stevens, B., Giorgetta, M., Esch, M., Mauritsen, T., Crueger, T., Rast, S., et al. (2013). Atmospheric component of the MPI-M earth system model: ECHAM6. *Journal of Advances in Modeling Earth Systems*, *5*(2), 146–172. https://doi.org/10.1029/2008jd010825

Stewart, M. K. (1975). Stable isotope fractionation due to evaporation and isotopic exchange of falling waterdrops: Applications to atmospheric processes and evaporation of lakes. *Journal of Geophysical Research*, *80*(9), 1133–1146. https://doi.org/10.1029/JC080i009p01133

Sun, C., Tian, L., Shanahan, T. M., Partin, J. W., Gao, Y., Piatrunia, N., & Banner, J. (2022). Isotopic variability in tropical cyclone precipitation is controlled by Rayleigh distillation and cloud microphysics. *Communications Earth & Environment*, *3*(1), 1–10. https://doi.org/10.1038/s43247-022-00381-1

Torri, G., Ma, D., & Kuang, Z. (2017). Stable water isotopes and large-scale vertical motions in the tropics. *Journal of Geophysical Research: Atmospheres*, *122*(7), 3703–3717. https://doi.org/10.1002/2016JD026154

Tremoy, G., Vimeux, F., Cattani, O., Mayaki, S., Souley, I., & Favreau, G. (2011). Measurements of water vapor isotope ratios with wavelength-scanned cavity ring-down spectroscopy technology: New insights and important caveats for deuterium excess measurements

in tropical areas in comparison with isotope-ratio mass spectrometry. *Rapid Communications in Mass Spectrometry*, *25*(July), 3469–3480. https://doi.org/10.1002/rcm.5252

Tremoy, G., Vimeux, F., Soumana, S., Souley, I., Risi, C., Favreau, G., & Oi, M. (2014). Clustering mesoscale convective systems with laser-based water vapor $\delta^{18}O$ monitoring in Niamey (Niger). *Journal of Geophysical Research: Atmospheres*, *119*(9), 1–25. https://doi.org/10.1002/2013JD020968

Tuinenburg, O. A., Risi, C., Lacour, J. L., Schneider, M., Wiegele, A., Worden, J., et al. (2015). Moist processes during MJO events as diagnosed from water isotopic measurements from the IASI satellite. *Journal of Geophysical Research: Atmospheres*, *120*(20), 10619–10636. https://doi.org/10.1002/2015JD023461

Vimeux, F. (2023). Is the isotopic composition of precipitation a robust indicator for reconstructions of past tropical cyclones frequency? A case study on Réunion Island from rain and water vapor isotopic observations (version 1). [Dataset]. Zenodo. https://doi.org/10.5281/zenodo.10057344

Vimeux, F., Gallaire, R., Bony, S., Hoffmann, G., & Chiang, J. C. H. (2005). What are the climate controls on deltaD in precipitation in the Zongo Valley (Bolivia)? Implications for the Illimani ice core interpretation. *Earth and Planetary Science Letters*, *240*(2), 205–220. https://doi.org/10.1016/j.epsl.2005.09.031

Vimeux, F., & Risi, C. (2021). Isotopic equilibrium between raindrops and water vapor Durinf the onset and the termination of the 2005-2006 wet season in the Bolivian Andes. *Journal of Hydrology*, *598*. 126472. https://doi.org/10.1016/j.jhydrol.2021.126472

Wang, G., Lan, H., & Liu, Z. (2021). Stable isotope record of super typhoon Lekima (2019). *Atmospheric Research*, *264*. 105822. https://doi.org/10.1016/j.atmosres.2021.105822

WMO. (2017). In C. Guard (Ed.), *Global guide to tropical cyclone forecasting* (p. 399). WMOTech. Rep.WMO/TD-1194. Retrieved from: http://www.wmo.int/cycloneguide/pdf/Global-Guide-to-Tropical-Cyclone-Forecasting.pdf

WMO. (2021). Atlas of mortality and economic losses from weather, climate and water extremes (1970–2019). WMO- N° 1267, ISBN 978-92-63-11267-5, published by WMO. Retrieved from: https://library.wmo.int/index.php?lvl=notice_display&id=21930#.Y0bGClLP2k4

Worden, J., Noone, D., & Bowman, K. (2007). Importance of rain evaporation and continental convection in the tropical water cycle. *Nature*, *445*(7127), 528–532. https://doi.org/10.1038/nature05508

Xu, T., Sun, X., Hong, H., Wang, X., Cui, M., Lei, G., et al. (2019). Stable isotope ratios of typhoon rains in Fuzhou, Southeast China, during 2013–2017. *Journal of Hydrology*, *570*, 445–453. https://doi.org/10.1016/j.jhydrol.2019.01.017

Yang, Z., Yuan, T., Jiang, H., Zhang, L., & Zhang, C. (2018). Stratiform and convective precipitation properties of tropical cyclones in the northwest Pacific. *Journal of Geophysical Research: Atmospheres*, *123*(7), 3513–3529. https://doi.org/10.1002/2017JD027174